Chinese Journal of Natural Medicines

Xijiaqi Formula attenuates cognitive dysfunction by inhibiting neuroinflammation and promoting neuroplasticity in rats with chronic heart failure

Jie Chen, Xuefen Wu, Qian Zhang, Hongcai Shang, Wanting Li, Linnan Zhou, Xinyu Chu, Guiyang Xia, Huan Xia, Xiaohong Wei, Sheng Lin

Citation: Jie Chen, Xuefen Wu, Qian Zhang, Hongcai Shang, Wanting Li, Linnan Zhou, Xinyu Chu, Guiyang Xia, Huan Xia, Xiaohong Wei, Sheng Lin, Xijiaqi Formula attenuates cognitive dysfunction by inhibiting neuroinflammation and promoting neuroplasticity in rats with chronic heart failure, Chinese Journal of Natural Medicines, 2026, 24(1), 73–88. doi: 10.1016/S1875–5364(26)61078–3.

View online: https://doi.org/10.1016/S1875–5364(26)61078–3

Wechat

Chinese Journal of Natural Medicines 24 (2026) 73-88

Contents lists available at ScienceDirect

Chinese Journal of Natural Medicines

journal homepage: www.cjnmcpu.com/

Original article

Xijiaqi Formula attenuates cognitive dysfunction by inhibiting neuroinflammation and promoting neuroplasticity in rats with chronic heart failure

Jie Chen[Δ], Xuefen Wu[Δ], Qian Zhang[Δ], Hongcai Shang, Wanting Li, Linnan Zhou, Xinyu Chu, Guiyang Xia, Huan Xia, Xiaohong Wei[*], Sheng Lin[*]

Key Laboratory of Chinese Internal Medicine of Ministry of Education and Beijing, Dongzhimen Hospital, Beijing University of Chinese Medicine, Beijing 100700, China

ARTICLE INFO

Article history:
Received 28 January 2025
Revised 2 April 2025
Accepted 30 June 2025
Available online 20 January 2026

Keywords:
Xijiaqi Formula
Cognitive dysfunction
Chronic heart failure
Synaptic plasticity
Neuroinflammation
PDE4

ABSTRACT

Chronic heart failure (CHF) impairs cognitive function. Xijiaqi Formula (XJQ), a traditional Chinese medicine (TCM) used clinically to treat CHF, demonstrates potential for improving cognition in CHF patients. However, its precise mechanism in treating post-CHF cognitive dysfunction remains unclear. This study systematically investigates XJQ's effects on post-CHF cognitive dysfunction and the underlying mechanisms. The components of XJQ were identified through liquid chromatography-mass spectrometry. CHF was induced in rats *via* ligation of the left anterior descending coronary artery, followed by six weeks of XJQ treatment. Cardiac function was evaluated through echocardiography and hemodynamic parameters, while cognitive function was assessed using Morris water maze (MWM) and open field tests (OFT). XJQ treatment enhanced both cardiac and cognitive functions in CHF rats. Network pharmacology identified 12 core active components of XJQ and indicated its effect on cognitive dysfunction involved regulating synapses, inflammation, and phosphodiesterase 4 (PDE4)-dependent cyclic adenosine monophosphate (cAMP) signaling. XJQ inhibited microglial and astrocyte activation, decreased proinflammatory cytokines, and mitigated neuronal damage. Notably, XJQ promoted synaptic repair and dendritic growth by downregulating PDE4 and upregulating cAMP, protein kinase A (PKA), cAMP-response element binding protein (CREB), brain-derived neurotrophic factor (BDNF), PSD95, and synapsin I levels. Molecular docking and Biolayer interferometry assays confirmed direct binding of quercetin, kaempferol, isorhamnetin, and darutoside to PDE4. In conclusion, XJQ alleviates neuroinflammation and enhances synaptic plasticity to improve cognitive dysfunction in CHF rats *via* the PDE4/cAMP/PKA/CREB signaling pathway. These findings provide valuable insight into the heart-brain axis.

1. Introduction

The heart and brain demonstrate extensive communication in pathophysiology, with cardiac activity significantly influencing cognitive processes including speech, feelings, and recall, as demonstrated by the heart-brain axis [1, 2]. Chronic heart failure (CHF) represents a syndrome of myocardial injury caused by various etiologies, resulting in myocardial structural and functional alterations that ultimately impair the heart's ability to pump or fill blood effectively. CHF affects millions globally, imposing a substantial burden on healthcare systems [3]. Beyond cardiac impairment, CHF causes systemic complications, notably cognitive dysfunction, which often receives insufficient attention [4]. Cognitive dysfunction in CHF patients ranges from memory and attention deficits to impaired executive function, significantly affecting their autonomy and adherence to complex treatment regimens [5].

The multifactorial pathophysiology connecting CHF to cognitive dysfunction encompasses ischemic brain changes due to reduced cardiac output, systemic inflammation, and neurohormonal imbalance [2, 6]. These factors collectively contribute to neurovascular instability and subsequent cognitive decline. However, the underlying mechanisms remain inadequately understood. Current CHF therapeutic approaches focus on improving cardiac function through pharmacological and non-pharmacological interventions, such as β-blockers and lifestyle modifications [7, 8]. Nevertheless, these approaches provide limited benefits for the cognitive aspects of CHF, creating a significant care gap. Additionally, the inadequately understood impact of CHF on cognitive function has impeded the development of targeted treatments.

Traditional Chinese medicine (TCM) offers a holistic approach with potential synergistic effects on both cardiac and cognitive functions [6, 9]. Xijiaqi Formula (XJQ), comprising Astragali Radix (Huangqi, HQ), Siegesbeckiae Herba (Xixiancao, XXC), and Periplocae Cortex (Xiangjiapi, XJP), serves specifically in clinical settings for CHF treatment. Recent research indicates that multiple XJQ components improve CHF through various targets including interleukin-6 (IL-6) and STAT3 [10]. Notably, XJQ demonstrates potential in improving post-CHF cognitive dysfunction (based on clinical data collection). Despite its clinical application, scientific understanding of XJQ's mechanisms regarding cognit-

* Corresponding author.
E-mail addresses: weixiaohong@bucm.edu.cn (X. Wei); lsznn@bucm.edu.cn (S. Lin)
Δ These authors contributed equally to this work.

https://doi.org/10.1016/S1875-5364(26)61078-3

ive functions remains limited.

This study aims to address this knowledge gap by investigating XJQ's effects on cognitive dysfunction in a rat model of CHF. The research focuses on examining XJQ's therapeutic potential, particularly its impact on neuroinflammation and synaptic plasticity. By elucidating the biological mechanisms through which XJQ influences the heart-brain axis, this study seeks to expand therapeutic options for CHF, potentially enhancing both cardiac and cognitive outcomes.

2. Materials and methods

2.1. Preparation of XJQ

Herbs of XJQ (HQ, 20210526; XXC, 830161101; and XJP, 181208) were obtained from Dongzhimen Hospital, Beijing University of Chinese Medicine (Beijing, China). Based on clinical dosage and herb compatibility ratio screening, XJQ was formulated using 40 g of HQ, 10 g of XXC, and 2.3 g of XJP. The herbs were immersed in ultrapure water at a ratio of 8 mL per gram of crude herbs for 2 h. The mixture underwent boiling for 45 min before filtration to obtain the filtrate. The residue was boiled again in ultrapure water for 25 min and filtered to obtain a second filtrate. The combined filtrates were lyophilized for subsequent use.

High-performance liquid chromatography (HPLC) was conducted using an Agilent 1260 Infinity II system equipped with a diode array detector on a C_{18} YMC ExRS column (column size: 250 mm × 4.6 mm, 5 μm; column temperature: 30 °C). Gradient elution employed acetonitrile (A) and water with 0.1% trifluoroacetic acid (B) at a flow rate of 1 mL·min^{-1} with the following schedule: 1) 0–8 min: from 10% to 95% A; 2) 8–30 min: from 95% to 60% A; 3) 30–40 min: from 60% to 0% A. The detailed acquisition conditions are provided in Table S1. Samples from two separate batches were analyzed to verify the chemical consistency of XJQ (Table S2 and Fig. S1).

2.2. Identification of components of XJQ

We dissolved 1 mg of herb powder in 1 mL of ultrapure water and filtered it through a 0.22 μm microporous membrane. The supernatant was collected and stored for ultra-high performance liquid chromatography-quadrupole/time-of-flight mass spectrometry (UPLC-Q/TOF-MS) analysis. The analysis was performed using an ACQUITY UPLC I Class system coupled with a Waters Synapt G2-Si Q-TOF system (Waters, Delaware, USA). Chromatographic separation utilized a Waters BEH C_{18} column (2.1 mm × 100 mm, 1.7 μm). Elution was conducted with a gradient at 40 °C and a flow rate of 0.3 mL·min^{-1}. The core ingredients of XJQ were identified using a Thermo Q-Exactive (UPLC-MS/MS) Orbitrap system. The injection volume was 3 μL, with additional UPLC-Q/TOF-MS conditions detailed in Table S3.

2.3. Animals and XJQ treatment

The experimental procedures followed the National Institutes of Health Guide for Care and Use of Laboratory Animals of China and adhered to the Animal Research: Reporting of *In Vivo* Experiments (ARRIVE) guidelines. Approval was obtained from the Experimental Animal Administration Committee at Dongzhimen Hospital of Beijing University of Chinese Medicine (approval No. 22-12). Male Sprague–Dawley rats (220 ± 10 g, SPF) were acquired from Vital River Laboratory Animal Technology Co., Ltd. (Beijing, China). They were maintained in a climate-controlled room with consistent temperature and humidity, a 12-h light/dark cycle, and unrestricted access to water and standard food.

The rats were anesthetized intraperitoneally with 1% pentobarbital (50 mg·kg^{-1}) and maintained on isoflurane while connected to ventilators (Alcott, ALC-V8). CHF models were induced by occluding the left anterior descending branch of the coronary artery, as previously described [11]. The heart was accessed *via* a left thoracotomy between the 3rd and 4th ribs. A 5-0 suture ligated the left anterior descending artery 3 mm from its origin, causing the left ventricular wall to lighten. After rapid hemostasis, the thoracic cavity was closed in layers. The Sham group underwent the same procedure without ligation. Rats that survived 24 h post-surgery with pathological *Q*-waves ≥ 6 on electrocardiograms were allocated into four groups [12]: CHF group, low dose XJQ + CHF group (XJQL, clinical equivalent dose), medium dose XJQ + CHF group (XJQM), and high dose XJQ + CHF group (XJQH). To convert the human dosage to an equivalent dose for rats, we employed an average adult body weight of 60 kg and a conversion factor of 6.3, which accounts for differences in metabolism and body surface area between humans and rats [13]. Therefore, the clinical equivalent dose (low dose) for rats was calculated as 5.45 g·kg^{-1}, and the medium and high doses were 2 and 4 times the clinical equivalent dose, respectively. Each experimental group received their specified dose by gavage daily for six weeks. The Sham and CHF groups received an equivalent volume of water.

2.4. Echocardiography and hemodynamic evaluations

Cardiac function was evaluated after 6 weeks of continuous treatment using echocardiography and hemodynamics as previously described [14, 15]. A 21-MHz phased-array probe (Vevo 2100, Visual Sonics Inc, Canada) measured the left ventricular ejection fraction (LVEF) and left ventricular fractional shortening (LVFS) values across 3 to 5 cardiac cycles.

Hemodynamic parameters were assessed after anesthetizing the rats and securing them in a supine position. A 2 cm segment of the right common carotid artery was exposed, with the distal end ligated and the proximal end clamped. A 1.5 mm incision was made near the ligature to insert a polyethylene catheter with a micro-pressure transducer. The clamp was then released to guide the catheter into the left ventricle. After 10 min of stabilization, left ventricular systolic pressure (LVSP), left ventricular end-diastolic pressure (LVEDP), maximal upstroke velocity of left ventricle ($+dp/dt_{max}$), and maximal descent velocity of left ventricle ($-dp/dt_{max}$) were recorded using BL-410S bio-function experiment system (Biopac, USA).

2.5. Behavior tests

The spatial memory and learning abilities of CHF rats were assessed using the Morris water maze (MWM) apparatus (XR-XM101, Shanghai, China) following established methodologies [16]. The test comprised two phases: an acquisition trial and a probe trial. During the acquisition trial, rats were randomly placed in the water from one of three quadrants that did not contain the platform. The trial concluded when the rats located the platform. If they failed to find it within 60 s, they were guided to it and allowed to remain for 10 s to reinforce learning. The time spent searching for the platform was recorded over 5 d. In the subsequent probe trial, the platform was removed, and rats were allowed to enter the pool from any of the three quadrants. The number of times they crossed the former platform location within a 60-s period was recorded.

Open field tests (OFT) were conducted to assess motor activity and exploratory behavior, utilizing SMART V3.0 software (Rayward, Shenzhen, China) [17]. To acclimate the rats to the experimenter's scent, they were exposed to it for 10 min daily over 5 d. Subsequently, the rats were given 1 h to adjust to the experimental room to minimize environmental disturbances. Each rat

was then placed individually in a sterilized open box with a black interior and subdued lighting. Their movements, including distance traveled, rest times, entries into the central zone, and time spent in the central zone, were recorded over a 5-min period. The box was cleaned after each session.

2.6. Nissl's staining

Brain sections were first deparaffinized and rehydrated before being stained with toluidine blue solution (Servicebio, Wuhan, China) for 15 min. After staining, the sections were washed with phosphate buffer, dehydrated with ethanol, and cleared with xylene. Images were captured using a 3Dhistech Pannoramic Scanner (3DHISTECH, Hungary). Finally, ImageJ software was employed for a blind analysis of Nissl bodies in the hippocampal regions CA1, CA3, and DG.

2.7. Network pharmacology analysis of XJQ and its effect of anti-cognitive dysfunction

2.7.1. Identification and collection of the components of XJQ and their targets

To obtain more comprehensive targets for XJQ components, in addition to the components identified by UPLC-Q/TOF-MS, additional components were screened from the TCMSP database (https://www.tcmsp-e.com/#/home), using criterion of oral bioavailability ≥ 30% and drug-likeness ≥ 0.18 [18]. Previously reported active components were also included, including isoliquiritigenin in HQ [19]; darutoside [20], rutin [21], isochlorogenic acid A, and isochlorogenic acid B [22] in XXC; and glycoside K, glycoside H1, glycoside H2 from XJP [23]. The TCMSP and SwissTargetPrediction databases (http://swisstargetprediction.ch/) were used to predict the targets of these active components.

2.7.2. Collection of targets of diseases

Targets for cognitive dysfunction were acquired using the keywords 'cognitive dysfunction' in the OMIM (https://omim.org. 2022-11-7) and GeneCards (https://www.genecards.org/. 2022-11-7) databases, with a relevance score > 20.

2.7.3. Construction of the component-disease-target network

A Venn diagram was generated using bioinformatics.com.cn to illustrate the shared targets between components and cognitive dysfunction. Cytoscape software was utilized to construct an interactive "herbs-components-targets-disease" network. In the "component-disease-target" network diagram, the 12 components with the highest degree values were identified as core active components of XJQ affecting cognitive dysfunction.

2.7.4. GO and KEGG analyses

David (https://david.ncifcrf.gov/) was employed for GO enrichment and KEGG analysis of mutual targets, with visualization performed using bioinformatics.com.cn.

2.7.5. Pharmacokinetic property analysis of core active components

Following the previous screening results, the 12 core active ingredients with the highest degree values underwent ADMET prediction. Their smiles formats were analyzed using the ADMETlab 2.0 platform to evaluate pharmacokinetic properties, including hERG blockers, H-HT, blood-brain barrier (BBB) penetration, plasma protein binding (PPB), anti-CYP enzyme metabolism effect, and clearance rate (CL). Safety assessment was conducted using the ROA test in rats.

2.8. Immunofluorescence staining

Brain tissue samples were fixed in formalin for 48 h, then embedded in paraffin and sectioned at 5 μm thickness. The sections were deparaffinized, rehydrated, and underwent antigen retrieval with sodium citrate solution for 20 min. Peroxidase activity was blocked with 3% H_2O_2 for 20 min. After a 1-h block in 5% BSA, sections were incubated overnight with anti-GFAP rabbit polyclonal antibody (1∶300, Proteintech, Wuhan, China) for astrocytes , anti-Iba-1 rabbit polyclonal antibody (1∶200, Wako, Japan) for microglia, synapsin I (1∶200, CST, USA), and PSD95 (1∶200, Selleck, USA). The next day, sections were incubated with goat anti-rabbit IgG (1∶500, Proteintech, Wuhan, China) as a secondary antibody for 1 h at 37 °C. Nuclear DNA was stained with DAPI (Boster Bio, USA). Images were captured using a fluorescence microscope at 200 × magnification (Leica, Germany).

2.9. Transmission electron microscopy (TEM)

Hippocampal tissue strips were sectioned into pieces no larger than 1 mm^3 and immediately fixed in 2.5% glutaraldehyde solution for 24 h. The tissues were subsequently washed in phosphate buffer, fixed in 1% osmium tetroxide, and dehydrated through increasing acetone concentrations. After embedding in epoxy resin, 80 nm sections were cut, stained with uranyl acetate and lead citrate, and divided into three blocks for ultra-thin slicing. These slices were examined using a transmission electron microscope (Hitachi, Japan).

2.10. Golgi staining and analysis

2.10.1. Golgi staining

Brains were extracted rapidly without perfusion and fixed in 4% formalin solution for 48 h. After fixation, 200 μm thick hippocampal sections were stained according to Safety Guidelines and Manufacturer's Instructions using the Golgi Stain Kit (Servicebio, Wuhan, China). Images were captured using the 3DHISTECH Pannoramic Scanner (3DHISTECH, Hungary). Three neurons per slice were selected for analysis based on their distinct structures and visible branches.

2.10.2. Neural analysis

Dendritic branch lengths were quantified using the Sholl analysis plugin in ImageJ software. This analysis involved counting intersections between dendrites and concentric circles centered on the neuron's cell body, with circles spaced 10 μm apart. Dendritic branching and length were determined by counting these intersections.

Dendritic spine density was evaluated on segments measuring at least 30 μm in length. Spines were categorized as mushroom, stubby, long, or filopodial-like, with mushroom and stubby types classified as mature. Spine density, both mature and immature, was calculated as spines per 10 μm of dendrite. These density calculations may underestimate actual values due to spines obscured by other dendrites not being included.

2.11. Cell culture and treatment

BV2 microglial and HT22 mouse hippocampal cell lines were cultured in high-glucose Dulbecco's modified Eagle's medium (DMEM) (Solarbio, Beijing, China) supplemented with 10% fetal bovine serum (Gibco, New York, USA) at 37 °C in a 5% CO_2 incubator. Lipopolysaccharide (LPS, Solarbio, Beijing, China) was dissolved in dimethyl sulfoxide to create a 1 $mg{\cdot}mL^{-1}$ stock solution, then diluted in DMEM to the required concentrations. BV2 cells were pre-treated with varying concentrations of XJQ, rolipram [a phosphodiesterase 4 (PDE4) inhibitor, 21.19 $\mu mol{\cdot}L^{-1}$], and MR-L2 (a PDE4 agonist, 3.18 $\mu mol{\cdot}L^{-1}$) for 3 h before a 24-h exposure

to 1 μg·mL^{-1} LPS.

2.12. Cell-cell interaction models

To investigate neuroinflammation-induced neuronal damage, a conditioned medium-based co-culture system of HT22 hippocampal cells and BV2 microglia was established.

2.12.1. Preparation of BV2-conditioned medium

Supernatants from BV2 cell cultures were collected at 90% confluence and centrifuged at 12 000 r·min^{-1} for 5 min. The clear supernatant was utilized immediately or stored at −80 °C. BV2 cell conditioned medium without LPS (C-CM) served as a control. LPS-stimulated conditioned medium (L-CM) was prepared by treating BV2 cells with LPS (1 μg·mL^{-1}) and collecting the medium after 24 h. L-CM with various concentrations of XJQ treatment (XJQ + L-CM) was also prepared.

2.12.2. HT22 cells were treated with BV2-conditioned medium

HT22 cells were seeded at 3.0 × 10^5 cells per well in 6-well plates and 8.0 × 10^3 cells per well in 96-well plates. Following attachment, the cells were treated with conditioned medium and incubated for 12 h. Morphological alterations in HT22 cells were evaluated using phase-contrast microscopy (Olympus, Japan).

2.13. Detection of NO

BV2 microglia were seeded at 1.0 × 10^4 cells per well in 96-well plates, pretreated with different concentrations of XJQ for 3 h, then exposed to 1 μg·mL^{-1} LPS for 24 h. Following treatment, the supernatant was collected, and NO levels were assessed using a NO detection kit according to the manufacturer's instructions (Beyotime, Shanghai, China). Absorbance at 540 nm was measured using a Rayto microplate reader (Shenzhen, China).

2.14. Cell viability assay of HT22 cells

The effect of BV2 cell-conditioned medium on HT22 cell viability was evaluated using the cell counting kit-8 assay. HT22 cells were co-cultured with BV2-conditioned medium for 12 h. Subsequently, 10 μL of the cell counting kit-8 reagent (Aoqing, Beijing, China) was added to each well and incubated at 37 °C for 3 h. Absorbance at 450 nm was measured using a Rayto microplate reader (Shenzhen, China).

2.15. Enzyme-linked immunosorbent assay (ELISA)

Blood samples were collected from abdominal veins and centrifuged at 3000 r·min^{-1} and 4 °C for 15 min to obtain serum. CHF severity was evaluated by measuring brain natriuretic peptide (BNP), *N*-terminal pro-B-type natriuretic peptide (NT-proBNP), angiotensin II (Ang II), cardiac troponin T (cTnT), and soluble ST2 (sST2) levels using ELISA kits (Dogesce, Beijing, China). Hippocampal tissue was isolated, homogenized, and centrifuged at 12 000 r·min^{-1} and 4 °C for 10 min to separate the supernatant. Tumor necrosis factor α (TNF-α), IL-1β, IL-10, protein kinase A (PKA), cyclic adenosine monophosphate (cAMP), and brain-derived neurotrophic factor (BDNF) levels in the hippocampus were determined using ELISA kits (Dogesce, Beijing, China). The culture medium from BV2 cells was centrifuged at 3000 r·min^{-1} at 4 °C for 15 min to obtain the supernatant. The concentrations of TNF-α and IL-1β in the supernatant were subsequently measured.

2.16. Western blot analysis

Iba1 and GFAP expression levels were measured to detect reactive microglia and astrocytes. Protein levels of PSD95, synapsin I, BDNF, PDE4, cAMP-response element-binding protein (CREB), and phosphorylated (p)-CREB were assessed in hippocampal tissue and HT22 cells. Total protein was extracted from the tissues and cells using RIPA lysis buffer (Beyotime, Shanghai, China). Protein concentrations were determined using a BCA protein assay kit (Beyotime, Shanghai, China). Proteins were separated by SDS-PAGE gels (30 μg/lane) and transferred to nitrocellulose membranes (Pall Corporation, USA). Membranes were blocked with 5% skim milk in TBST for 90 min, then incubated overnight at 4 °C with primary antibodies against PSD95 (1∶1000, Proteintech, Wuhan, China), synapsin I (1∶1000, CST, USA), Iba1 (1∶1000, Proteintech, Wuhan, China), GFAP (1∶1000, Proteintech, Wuhan, China), BDNF (1∶1000, Abways, Shanghai, China), PDE4 (1∶1000, Immunoway, USA), CREB (1∶1000, Proteintech, Wuhan, China), p-CREB (1∶1000, Proteintech, Wuhan, China), and *β*-actin (1∶8000, Abclonal, Wuhan, China). After washing, membranes were incubated with secondary antibodies for 90 min. The results were visualized using an enhanced chemiluminescence system (Lablead, Beijing, China), and optical density was quantified using ImageJ.

2.17. Molecular docking

The structure of the core components from Section "2.6.1" was obtained from TCMSP (https://old.tcmsp-e.com/tcmsp.php) in MOL2 format. Using AutoDockTools-1.5.7, these structures were converted to pdbqt format to generate ligands. Water molecules and other ligands were removed from the target PDB files (sourced from the PDB, http://www.rcsb.org/) using PyMOL. Additional processing with AutoDockTools-1.5.7 included hydrogenation, conversion to pdbqt format, and marking of receptor active sites. Molecular docking was performed using AutoDock Vina to calculate binding energies. The results were visualized using PyMOL and LigPlot+.

2.18. Bio-layer interferometry (BLI) assay

The interaction between 12 components of XJQ and PDE4 was analyzed using BLI technology, which employs light interference signals, non-labeling, and real-time monitoring to ensure experimental reliability. The BLI assay was conducted on a FORTEBlO Octet K2 system. Each well in a 96-well plate contained 200 μL of assay buffer. Four super streptavidin (ssA)-labeled probes were selected, with control sensors without immobilized proteins established to enhance binding/dissociation specificity. The probes were pre-wetted in 5% PBS buffer for 10 min; protein solution was prepared at 400 μg·mL^{-1}. The baseline was established for 120 s for equilibration, the protein was immobilized for 600 s, and re-equilibrated for 120 s to establish a new, stable baseline signal. The probes were exposed to each component solution at different final concentrations for 60 s. Subsequently, the bound probes underwent a 60-s dissociation phase in the buffer. Following BLI principles, the magnitude of the signal response served as the basis for assessment. Affinity constants (K_d values) were calculated to evaluate intermolecular interaction strength, with smaller K_d values indicating greater affinity.

2.19. Statistical analysis

Statistical analyses and data visualization were conducted using GraphPad Prism 8.0 (GraphPad Software, La Jolla, CA, USA). The two-tailed *t*-test was utilized for comparisons between two groups, and the one-way analysis of variance (ANOVA) followed by Dunnett's test was applied for comparisons among three or more groups. Results were expressed as mean ± standard error of mean (SEM), with $P < 0.05$ considered statistically significant.

3. Results

3.1. XJQ treatment improves cardiac function after myocardial infarction

To investigate the effects of XJQ on cardiac function in CHF rats post-myocardial infarction, echocardiography was performed to assess LVEF and LVFS as indicators of myocardial contractility (Fig. 1A). The CHF group demonstrated significant decreases in LVEF and LVFS compared to the Sham group, indicating impaired cardiac function following myocardial infarction. XJQ treatment significantly enhanced both LVEF and LVFS (Figs. 1B–1D). Additionally, XJQ substantially improved cardiac diastolic dysfunction in the CHF group. These improvements were supported by positive changes in hemodynamic parameters, including elevated LVSP, $+dp/dt_{max}$, reduced LVEDP, and increased absolute value of $-dp/dt_{max}$ (Figs. 1E–1H).

Cardiac biomarkers including BNP, NT-proBNP, and cTnT are established diagnostic indicators for CHF, as their levels increase in affected patients. CHF severity was assessed through measurement of BNP, NT-proBNP, and cTnT levels in serum. The CHF group exhibited significantly elevated levels of these biomarkers compared to the Sham group. XJQ treatment effectively reduced BNP, NT-proBNP, and cTnT levels in the CHF group (Figs. 1I–1K). Ang II, a hormone promoting vasoconstriction and cardiac hypertrophy [24], and sST2, a sensitive marker of myocardial fibrosis and ventricular remodeling, were both increased in CHF rats [25]. XJQ treatment successfully mitigated the elevation of sST2 and Ang II levels induced by CHF (Figs. 1L and 1M). These findings collectively demonstrate the significant cardioprotective effects of XJQ in enhancing cardiac contractility and diastolic function, while reducing vasoconstriction, cardiac hypertrophy, and ventricular remodeling.

3.2. XJQ treatment alleviates hippocampus-dependent learning and memory dysfunction in CHF rats

The MWM test was employed to assess learning and memory in CHF rats. During the acquisition trial, the escape latency and total swimming distance decreased from the 1st day to the 5th day, with no significant differences observed. Swimming speed remained consistent across all groups (Figs. 2A–2C). In the probe trial, CHF rats showed decreased platform crossings, time, and distance spent in the target quadrant compared to the Sham group, while XJQ treatment enhanced these parameters (Figs. 2D–2G). These results demonstrate that CHF significantly impairs spatial learning and memory, an effect partially reversed by

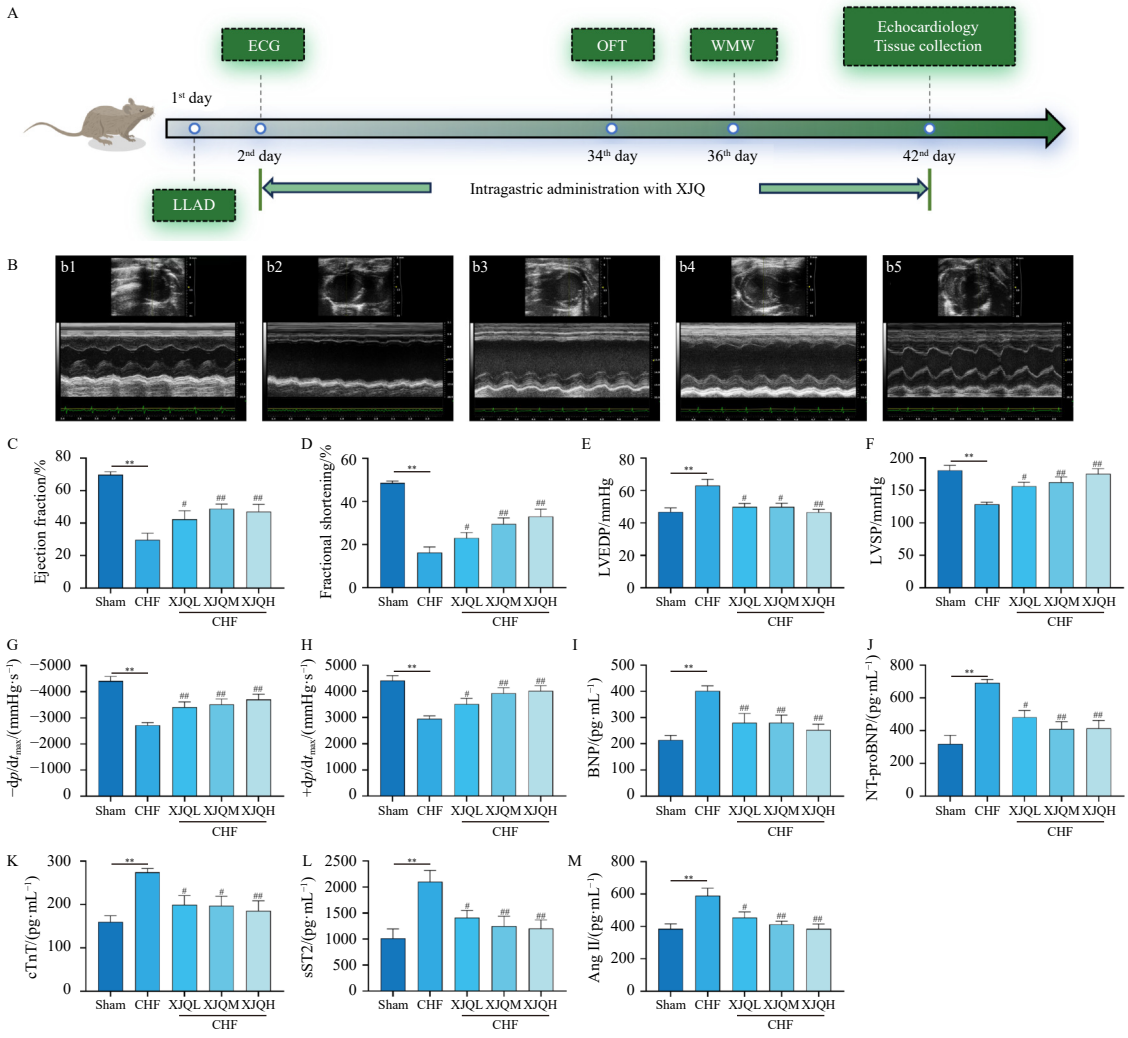

Fig. 1 XJQ significantly improves cardiac function and hemodynamic indices in CHF rats following myocardial infarction. (A) Animal experiment schedule. (B) Representative M-mode echocardiograms (b1: Sham group, b2: CHF group, b3: CHF + XJQL group, b4: CHF + XJQM group, b5: CHF + XJQH group). (C and D) Quantification of LVEF (C), LVFS (D), based on echocardiography. (E–H) Quantification of cardiac hemodynamic indices, including LVEDP (E), LVSP (F), $-dp/dt_{max}$ (G), $+dp/dt_{max}$ (H). (I–M) Serum levels of BNP (I), NT-proBNP (J), cTnT (K), sST2 (L) and Ang Ⅱ (M) were detected using ELISA. Data are presented as the mean ± SEM (n = 6). $^{*}P < 0.05$, and $^{**}P < 0.01$ *vs* Sham; $^{\#}P < 0.05$, and $^{\#\#}P < 0.01$ *vs* CHF. LADL: ligating the left anterior descending branch coronary artery; ECG: electrocardiography; OFT: open field test; WMW: Morris water maze.

XJQ treatment.

The OFT results revealed significant decreases in total distances, distances in the center, frequency of center entries, and average speed in CHF rats compared to the Sham group (Figs. 2H–2K). XJQ treatment significantly improved these parameters in the CHF group, suggesting partial restoration of locomotor activity. These behavioral assessments indicate that CHF serves as a substantial risk factor for learning and memory impairments, while XJQ treatment provides measurable relief from these cognitive deficits.

3.3. XJQ treatment mitigates the loss and damage of neurons in the hippocampus

Nissl bodies play a crucial role in synthesizing essential components for neuronal health, including structural proteins, enzymes involved in neurotransmitter synthesis, and neuromodulatory peptides [26]. Neuronal damage is manifested by the reduction, disintegration, or loss of Nissl bodies. The Sham group displayed densely arranged nerve cells with abundant Nissl bodies in CA1, CA3, and DG regions. In contrast, the CHF group exhibited lighter cytoplasm and decreased Nissl bodies in these regions (Figs. 3A–3D). XJQ treatment prevented the reduction in both Nissl body quantity and staining intensity compared to the CHF group.

TEM analysis revealed intact neural structure and normal organelle morphology in the Sham group. The CHF group demonstrated severe neural edema, localized cell membrane breakage, free organelles, extensive low electron density edema, mitochondrial matrix lysis, and significant organelle swelling. Mitochondria (red arrow) in the CHF group deteriorated into vacuoles, exhibiting disintegrated mitochondrial matrix and disappearing cristae (Fig. 3E). XJQ treatment reduced neuronal edema and structural damage, while partially restoring mitochondrial and neural ultrastructure compared to the CHF group, indicating XJQ's protective effect on hippocampal neuronal integrity.

3.4. Component-disease-target network and function of target analysis of XJQ to combat cognitive dysfunction

We analyzed the potential targets and pathways of XJQ for treating cognitive dysfunction using network pharmacology. Initially, component analysis of XJQ was performed with UPLC-Q/TOF-MS, yielding total ion chromatogram for both positive and negative ion modes (Figs. S2A and S2B). The exact mass-to-charge ratio (m/z) and retention time of each compound were obtained *via* TOF-MS, while secondary fragment ions were acquired through product ion secondary mass spectrometry. Through online databases, literature review of the three constituent herbs of XJQ (HQ, XXC, XJP), and compound fragmentation patterns, 29 XJQ-related components were identified (Table S4). Beyond these 29 components, additional screening using the TCMSP database with criteria of oral bioavailability ≥ 30% and drug-like properties ≥ 0.18 identified 52 components, with 2 components common across all three herbs (Fig. 4A and Table S5). The analysis mapped 433 targets from these components (Table S6) and identified 852 targets for cognitive dysfunction (Table S7). A Venn diagram revealed 46 mutual targets between XJQ and cognitive dysfunction (Fig. 4B and Table S8). Active components and targets were imported into Cytoscape to construct an herb-component-disease-target network, demonstrating interactions between each herb and multiple cognitive dysfunction targets (Fig. 4C), suggesting therapeutic potential. Interaction analysis identified 34 active components associated with cognitive dysfunction targets: 10 from herb XXC, 11 from herb HQ, and 13 from herb XJP. Based on network centrality degree, 12 components were identified as core active components in XJQ for treating cognitive dysfunction (Table 1). ADMET results serve as crucial reference indices for compound druggability. The ADMET-

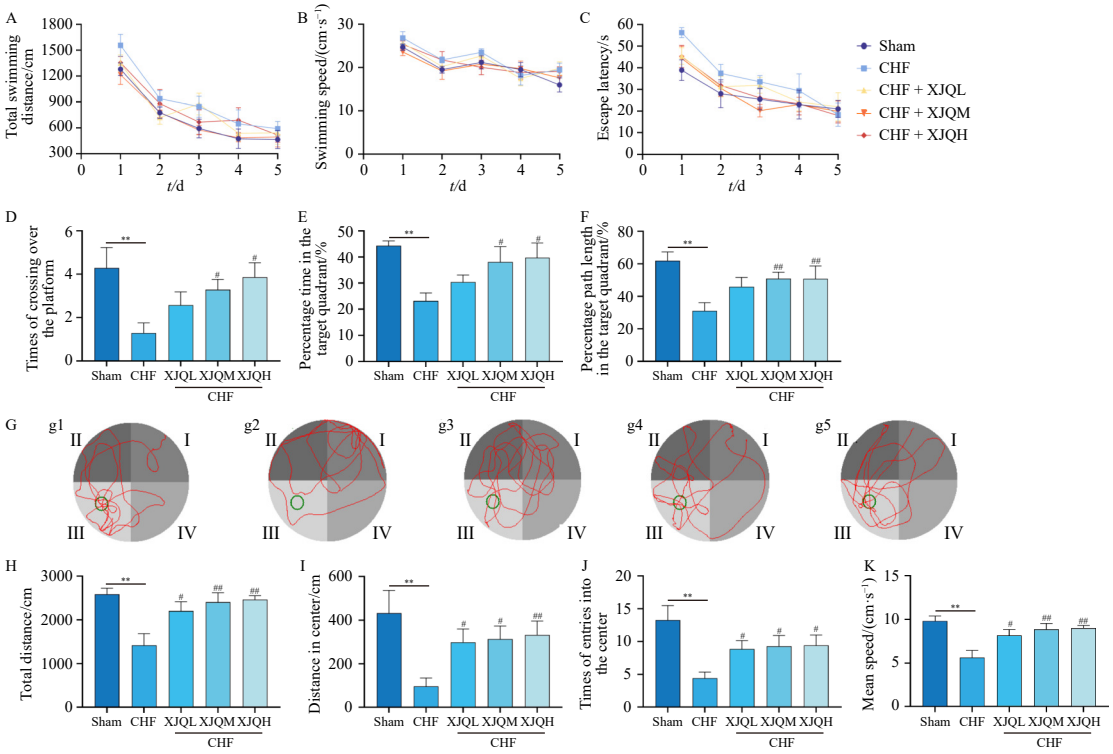

Fig. 2 XJQ alleviates cognitive performance deficits in CHF rats. (A–C) The acquisition trial of Morris water maze, included total average swimming distance (A), average swimming speed (B), escape latency for rats to find the underwater platform (C). (D–F) The probe trial of Morris water maze, included times of crossing over the platform (D), percentage of the time (E) and distance (F) spent in the target quadrant. (G) Representative track images from the spatial probe trails. (H–K) The parameters of open field test, included total distance (H), distance in the center (I), times of entries into the center (J), and mean speed (K). Data are presented as the mean ± SEM (n = 10). $^{*}P$ < 0.05, and $^{**}P$ < 0.01 *vs* Sham; $^{\#}P$ < 0.05, and $^{\#\#}P$ < 0.01 *vs* CHF.

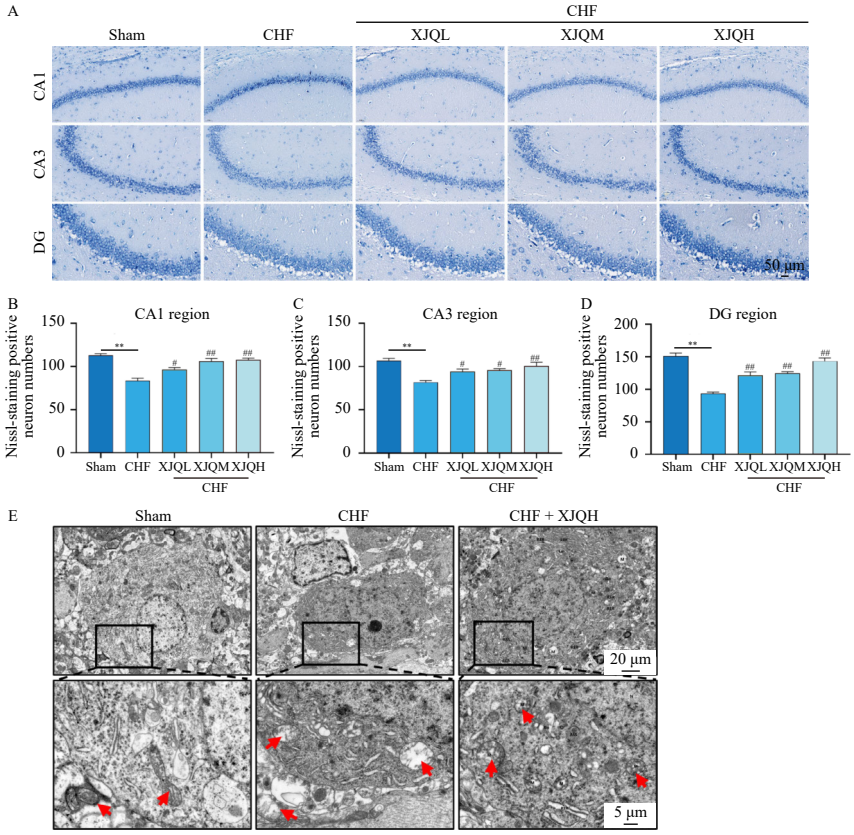

Fig. 3 XJQ mitigates the loss of Nissl bodies and ultrastructural damage in the hippocampal neurons of CHF rats. (A–D) Representative images of Nissl staining (A) and quantification of Nissl bodies in CA1 (B), CA3 (C), DG (D) regions of the hippocampus (n = 4). (E) Representative transmission electron microscope images of neurons shown at magnification × 2500, scale bars: 20 μm; magnification × 8000, scale bars: 5 μm (n = 3). Data are presented as the mean ± SEM; $^{*}P < 0.05$, and $^{**}P < 0.01$ *vs* Sham; $^{\#}P < 0.05$, and $^{\#\#}P < 0.01$ *vs* CHF.

lab 2.0 platform provided predictions of pharmacokinetic properties, including absorption, distribution, excretion, and toxicity (Tables 1 and S7). Neridienone A, stigmasterol, and coronaridine demonstrate excellent BBB penetration. ROA represents a critical safety parameter for drug candidates [27]. ADMET findings indicate that 8 of the 12 core active ingredients in XJQ are non-toxic and therapeutically beneficial.

We performed GO enrichment and KEGG analyses on the 46 mutual targets to investigate the mechanisms underlying XJQ's impact on cognitive dysfunction. The top 30 GO enrichment results demonstrated that the regulation of signal transduction, inflammation, and synapses are fundamental to XJQ's effectiveness in ameliorating cognitive dysfunction (Fig. 4D). The top 20 KEGG results indicated that XJQ enhances cognitive function through multiple pathways, with cAMP signaling playing a crucial role (Fig. 4E). cAMP functions as an intracellular second messenger, and its modification affects downstream intracellular signaling.

3.5. XJQ treatment alleviates neuroinflammatory response via inhibiting the activation of microglia and astrocytes in the hippocampus

Based on network pharmacology predictions, we implemented various molecular biology assays. We evaluated the content of inflammatory cytokines in the hippocampal region. TNF-α and IL-1β are established proinflammatory cytokines. Compared to the Sham group, CHF significantly elevated IL-1β and TNF-α, and slightly increased IL-10 in the hippocampus (Figs. 5A–5C). XJQ treatment effectively lowered TNF-α and IL-1β levels in a dose-dependent manner compared to the CHF group. IL-10 is an anti-inflammatory cytokine. High doses of XJQ significantly enhanced IL-10 release. XJQ maintains equilibrium between proinflammatory and anti-inflammatory pathways to reduce neuroinflammation.

The activation of microglia and astrocytes represents key contributors to inflammation in the CNS, with Iba1 and GFAP serving as markers of their activation, respectively. The Sham group demonstrated low fluorescence intensity in Iba1-positive microglia and GFAP-positive astrocytes, whereas the CHF group showed increased intensity (Figs. 5D–5F). XJQ administration reversed the elevation in fluorescence intensity of Iba1-positive microglia and GFAP-positive astrocytes in the hippocampus. These observations were further validated by Western blot analysis (Figs. 5G–5I), confirming that XJQ effectively suppressed the activation of microglia and astrocytes triggered by CHF, thereby reducing hippocampal neuroinflammatory responses.

3.6. XJQ treatment restores synaptic ultrastructure, synaptic plasticity, and regulated cAMP signaling pathway

To comprehensively examine the effects of XJQ on hippocampal synaptic plasticity in CHF rats, we evaluated synaptic ultrastructure changes and quantified key synaptic proteins (PSD95 and synapsin I). Synapses comprise distinct anterior and posterior membranes, termed the presynaptic active region and postsynaptic density (PSD), respectively. The length of the presynaptic active region indicates the effective region of neurotransmitter release. Tubulin and actin constitute primary components of the proteins (PSD), and their thickness correlates closely with synaptic function and plasticity. Synaptic curvature substantially influences synaptic function. Enzymes in the synaptic cleft degrade neurotransmitters, and the width of the cleft inversely affects the efficiency of neurotransmitter transmission. Representative images of synaptic density and interface parameters are shown in Fig. 6A. Quantitative analysis revealed that CHF rats exhibited reduced synaptic density (Fig. 6B), thinner PSD thickness

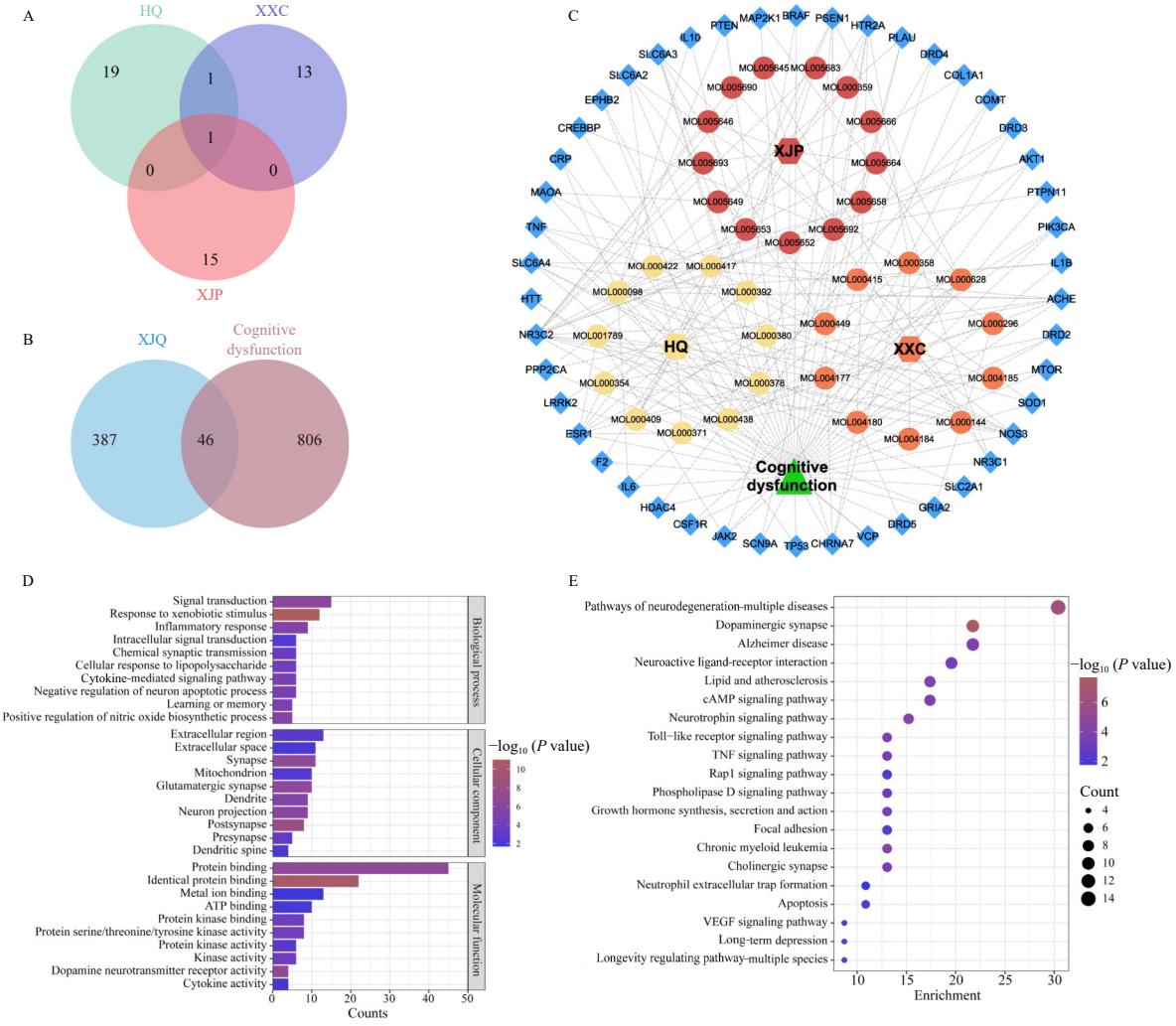

Fig. 4 Network pharmacology analysis reveals that the efficacy of XJQ focuses on inflammation and synapses, involving cAMP signaling. (A) A Venn diagram of the components from HQ, XXC, and XJP in XJQ. (B) A Venn diagram showing the 46 common targets between XJQ and cognitive dysfunction. (C) The component-disease-target network of XJQ for cognitive dysfunction, depicted using a correlation analysis between the components' targets and the targets of cognitive dysfunction (Red triangles represent cognitive dysfunction, circles represent active components in XJQ-yellow for HQ, orange for XXC, red for XJP, and blue rhombus represent the 46 potential targets). (D) The top 30 GO terms of common targets, including biological process (BP), cellular component (CC), molecular function (MF). (E) The top 20 KEGG pathways of common targets.

Table 1 Core active components of XJQ for cognitive dysfunction.

MOL ID	Name	Chemical formula	CAS ID	Topological coefficient	Closeness centrality	Degree	hERG Blockers	H-HT	ROA	BBB penetration	Source
MOL000098	Quercetin	$C_{15}H_{10}O_7$	117-39-5	0.214 286	0.365 639	15	-	-	-	---	HQ
MOL005692	Neridienone A	$C_{21}H_{26}O_3$	53823-05-5	0.170 29	0.389 671	12	---	--	+	+++	XJP
MOL000438	(*R*)-Isomucronulatol	$C_{17}H_{18}O_5$	64474-51-7	0.190 909	0.336 032	11	---	--	-	---	HQ
MOL000449	Stigmasterol	$C_{29}H_{48}O$	83-48-7	0.206 731	0.386 047	8	---	---	---	+	XXC
MOL000628	Darutoside	$C_{26}H_{44}O_8$	59219-65-7	0.238 095	0.341 564	6	---	--	+	--	XXC
MOL004180	Coronaridine	$C_{21}H_{26}N_2O_2$	467-77-6	0.297 619	0.336 032	6	-	-	+++	+++	XXC
MOL000378	7-*O*-Methy-lisomucronulatol	$C_{18}H_{20}O_5$	137217-83-5	0.385 417	0.347 28	6	--	--	--	---	HQ
MOL000422	Kaempferol	$C_{15}H_{10}O_6$	520-18-3	0.355 556	0.344 398	6	---	---	--	---	HQ
MOL000392	Formononetin	$C_{16}H_{12}O_4$	485-72-3	0.395 833	0.347 28	6	--	---	--	--	HQ
MOL000409	Astragaloside IV	$C_{41}H_{68}O_{14}$	83207-58-3	0.270 588	0.347 28	5	---	--	++	---	HQ
MOL000415	Rutin	$C_{27}H_{30}O_{16}$	153-18-4	0.3	0.328 063	5	---	---	---	--	XXC
MOL000354	Isorhamnetin	$C_{16}H_{12}O_7$	480-19-3	0.492 308	0.336 032	5	---	---	---	---	HQ

hERG Blockers: human ether-a-go-go related gene; H-HT: human hepatotoxicity; ROA: rat oral acute toxicity; BBB penetration: blood-brain barrier penetration. The output value was the probability of toxicity in the range of 0–1. For the classification endpoints, the prediction probability values are transformed into six symbols: 0–0.1 (---), 0.1–0.3 (--), 0.3–0.5 (-), 0.5–0.7 (+), 0.7–0.9 (++), and 0.9–1.0 (+++).

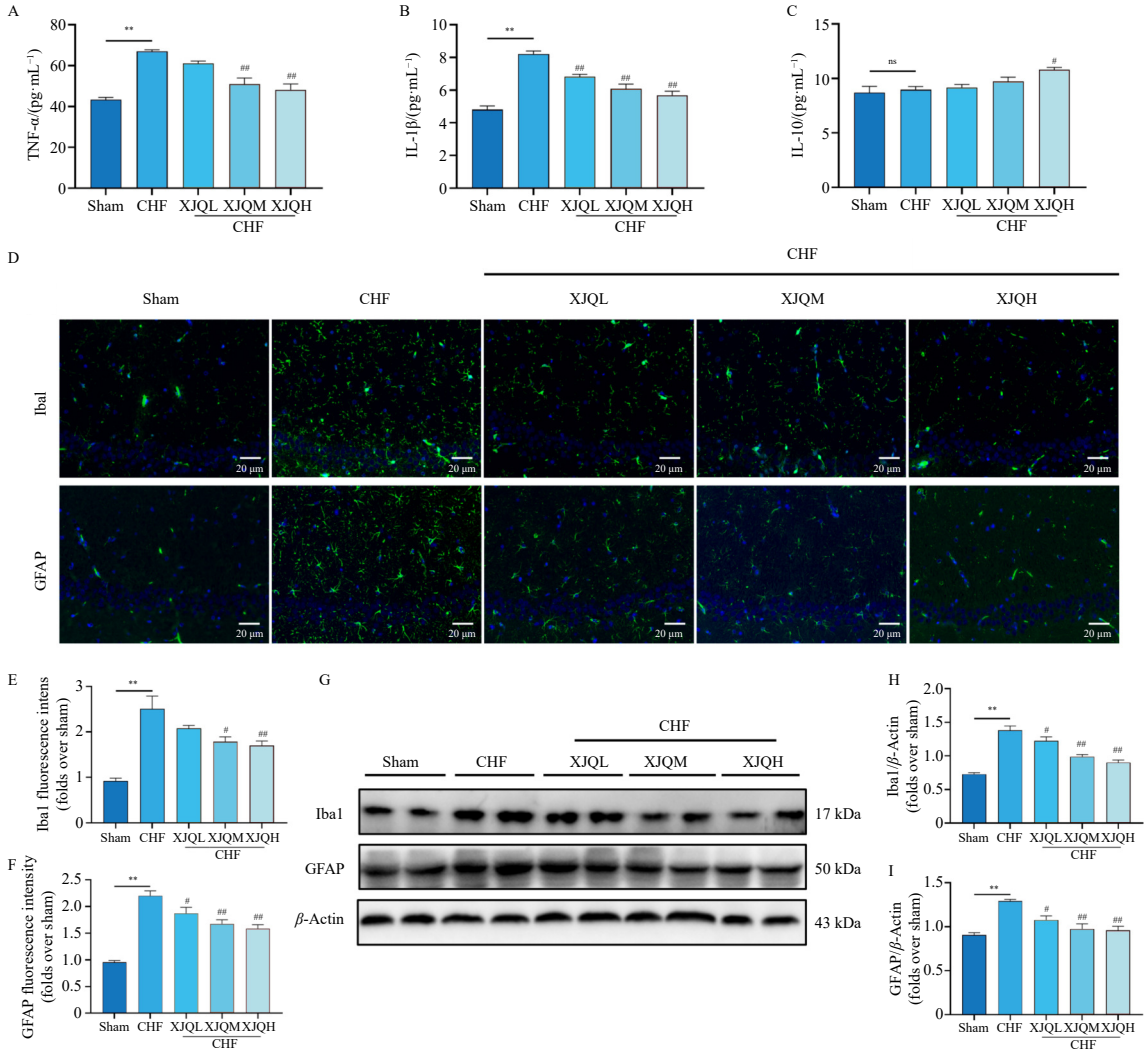

Fig. 5 XJQ alleviates the inflammatory responses *via* inhibiting the activation of microglia and astrocytes in the hippocampus. (A–C) Levels of TNF-α (A), IL-1β (B), and IL-10 (C) in the hippocampus were detected by ELISA (n = 6). (D–F) Representative images of Iba1 and GFAP staining in the hippocampus (D) and their quantitative analysis of fluorescence intensity (E and F). Green: Iba1 or GFAP; Blue: DAPI (n = 4; Scale bar, 20 μm). (G–I) Representative Western blots (G) and quantification data for Iba1/β-Actin (H) and GFAP/β-Actin (I). β-Actin was used as a loading control (n = 4). Data are presented as the mean ± SEM; $^{*}P < 0.05$, and $^{**}P < 0.01$ *vs* Sham; $^{\#}P < 0.05$, and $^{\#\#}P < 0.01$ *vs* CHF.

(red arrow) (Fig. 6C), shorter active zone length (red arrow) (Fig. 6D), and wider synaptic clefts (Fig. 6E) compared to the Sham group. XJQ treatment significantly increased synaptic density, PSD thickness, and active zone length, while reducing synaptic cleft width. No significant differences in synaptic curvature (red arrow) were observed among the three groups (Fig. 6F).

PSD95 functions as a critical marker of the postsynaptic membrane and demonstrates high abundance in the PSD. Synapsin I operates as a regulator of synaptic vesicle trafficking and modulates neurotransmitter release in presynaptic terminals. The CHF group demonstrated a significant reduction in PSD95 and Synapsin I levels relative to the Sham group (Figs. 6G–6I). XJQ treatment effectively mitigated the CHF-induced decreases in PSD95 and synapsin I expression. These observations were corroborated by immunofluorescence analysis, which revealed significantly diminished fluorescence intensity of PSD95 and synapsin I in the CHF group compared to the Sham group, with subsequent enhancement following XJQ treatment (Figs. 6J–6L).

PDE4, a key enzyme responsible for cAMP hydrolysis, plays a fundamental role in regulating neurogenesis and synaptic plasticity *via* cAMP signaling. Network pharmacology analysis indicates that PDE4-dependent cAMP signaling represents a critical mechanism underlying XJQ's therapeutic efficacy in cognitive dysfunction. The CHF group displayed increased PDE4 protein levels compared to the Sham group, which were subsequently reduced by XJQ treatment (Figs. 6M and 6N). PDE4-mediated cAMP hydrolysis maintains appropriate cAMP levels, and both cAMP content and PKA activity showed reduction in the CHF group (Figs. 6P and 6Q), aligning with cAMP's role in PKA activation. XJQ administration enhanced hippocampal cAMP content and PKA activity relative to the CHF group. Additionally, the CHF group exhibited decreased p-CREB protein expression compared to the Sham group, which was subsequently elevated by XJQ treatment (Figs. 6M and 6O).

BDNF plays an essential role in mediating long-term potentiation (LTP) and long-term depression, promoting neuronal synaptogenesis, and enhancing hippocampal synaptic plasticity [28]. The CHF group showed reduced BDNF levels compared to the Sham group (Fig. 6R). These results indicate that CHF induces synaptic loss and compromises synaptic ultrastructure in the hippocampal region. XJQ facilitates synaptic structural repair and protein restoration through regulation of the PDE4/cAMP/PKA/CREB pathway.

3.7. XJQ treatment promotes the growth of dendrites and dendritic spines in the hippocampus

The dynamic nature of dendritic spines is fundamental to

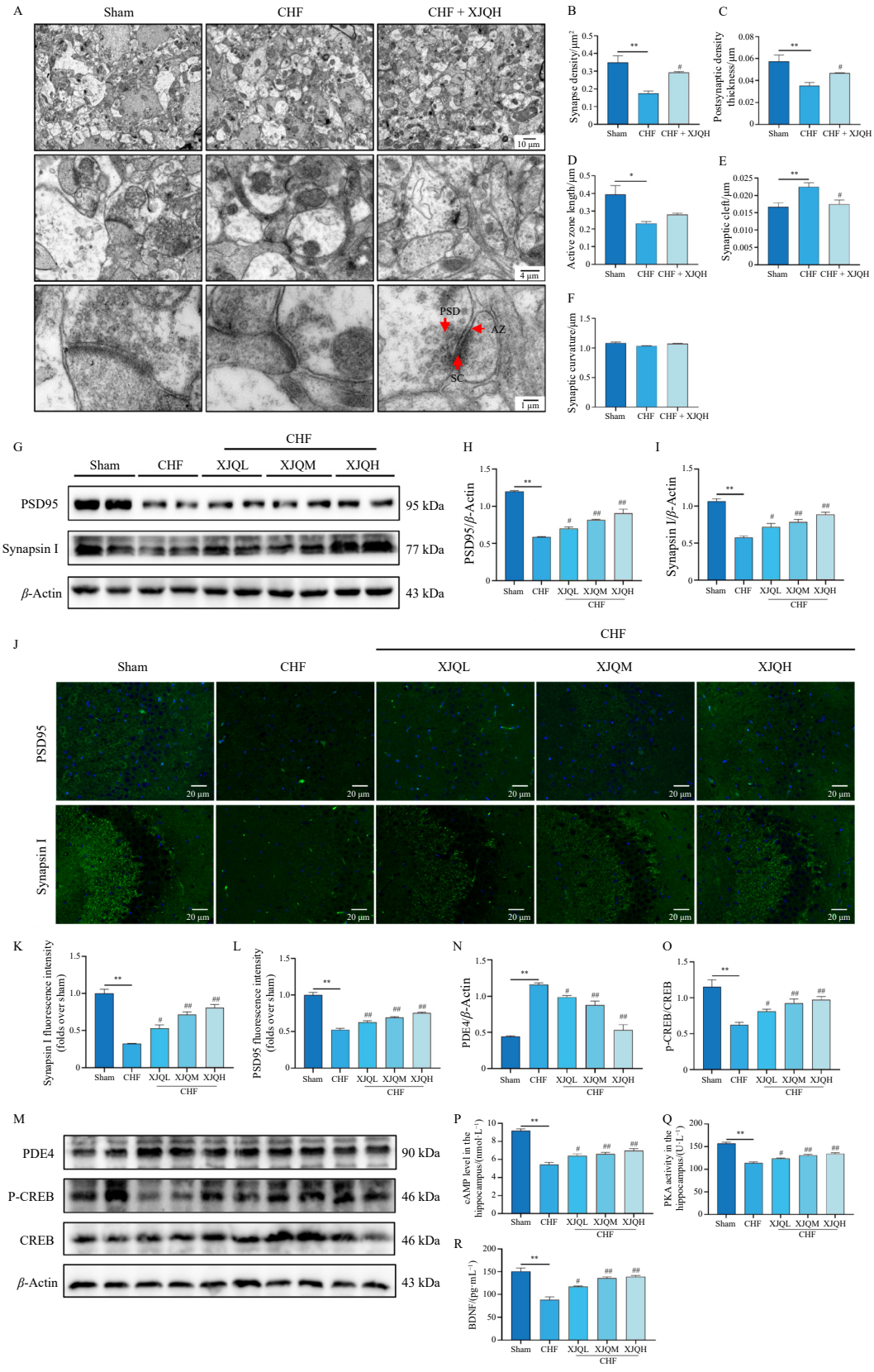

Fig. 6 XJQ eases the impairment of synaptic plasticity and regulates PDE4/cAMP/PKA/CREB signaling in the hippocampus of CHF rats. (A) Representative transmission electron microscope images of synapses in the hippocampus shown at magnification × 4000, scale bars: 10 μm; × 15 000, scale bars: 4 μm; × 50 000, scale bars: 1 μm. (B–F) Quantification of the synaptic interfaces, including synapse density (B), PSD thickness (C), active zone length (D), synaptic cleft (E) and synaptic curvature (F) (n = 3). (G–I) Representative Western blots (G) and quantification data of PSD95 (H), synapsin I (I). β-Actin was used as a loading control (n = 4). (J–L) Representative immunofluorescence images of PSD95 and synapsin I in the hippocampus (J) and their quantitative analysis of fluorescence intensity (K–L). Green: PSD95 or synapsin I; Blue: DAPI. Scale bar, 20 μm. (M–O) Representative Western blots (M) and quantification data of PDE4 (N), p-CREB and CREB (O). β-Actin was used as a loading control (n = 4). (P–R) The content of cAMP (P), the activity of PKA (Q), and BDNF content (R) in the hippocampus, detected by ELISA (n = 6). Data are presented as the mean ± SEM; $^{*}P < 0.05$, and $^{**}P < 0.01$ *vs* Sham; $^{\#}P < 0.05$, and $^{\#\#}P < 0.01$ *vs* CHF. PSD: postsynaptic density; AZ: active zone length; SC: synaptic curvature.

structural synaptic plasticity, which supports cognition and memory [29]. This investigation evaluated dendritic parameters, including the total number of intersections, count, and total length of dendritic branches within the hippocampus to determine the effects of CHF and XJQ on dendritic growth. Golgi staining was employed to visualize dendritic shafts and spines of neurons (Figs. 7A–7C). Sholl analysis demonstrated that CHF significantly decreased the total number of intersections compared to the Sham group (Figs. 7D and 7E). Following XJQ treatment, the total number of intersections increased significantly, indicating more extensive and complete neuronal branching compared to the CHF group. Additionally, CHF significantly reduced both the number and total length of dendritic branches compared to the Sham group (Figs. 7F and 7G). XJQ treatment effectively restored both the total number and length of branches.

Modifications in dendritic spine morphology influence synaptic function, neural circuit connectivity patterns, and cognitive behavior. The study examined microstructural changes in dendritic spines within the hippocampus. The density of mature and immature spines was assessed using a traditional classification of spine morphology (Fig. 7H). Representative images of Golgi-stained dendritic spines from the hippocampus are shown in Fig. 7I. Immature dendritic spines are associated with learning behaviors, while mature spines facilitate memory storage. The CHF group demonstrated a significant reduction in both total spine density and mature spines compared to the Sham group (Figs. 7J and 7K). Following XJQ treatment, both total spine density and the number of mature spines were significantly higher than in the CHF group. Furthermore, CHF marginally decreased the number of immature spines (Fig. 7L). XJQ treatment moderately increased the density of immature spines that had diminished in the CHF group.

3.8. XJQ alleviates the damage of inflammation produced by microglia to neurons via PDE4-mediated cAMP signaling

To investigate how XJQ-modulated neuroinflammation affects neuronal growth and synaptic plasticity, a co-culture system comprising BV2 microglia and HT22 hippocampal neurons was established. This model simulates the brain's inflammatory microenvironment (Fig. 8A). The CCK8 assay results indicated that XJQ concentrations ranging from 5 to 50 μg·mL^{-1} exhibited no significant effect on cell viability (Fig. S3A). NO, TNF-α, and IL-1β levels were measured in the culture medium of BV2 cells following LPS stimulation. The LPS group showed elevated levels of these markers compared to the control group. XJQ treatment effectively reduced NO, IL-1β, and TNF-α in a dose-dependent manner (Figs. S3B–S3D).

The viability of HT22 cells was significantly reduced by LPS-treated BV2 cells; however, XJQ treatment effectively restored cell viability (Fig. 8B). Microscopic examination revealed that HT22 cells exposed to medium from LPS-treated BV2 cells displayed abnormal morphology, characterized by distortion, shrinkage, fragmentation, and cell death. Treatment with XJQ substantially improved the morphological characteristics of these HT22 cells (Fig. 8C). Western blot analysis demonstrated reduced levels of PSD95, synapsin I, and BDNF in HT22 cells exposed to LPS-treated BV2 medium, which XJQ treatment effectively reversed (Figs. 8D–8F and 8I). Additionally, LPS-treated BV2 medium induced increased PDE4 expression and decreased

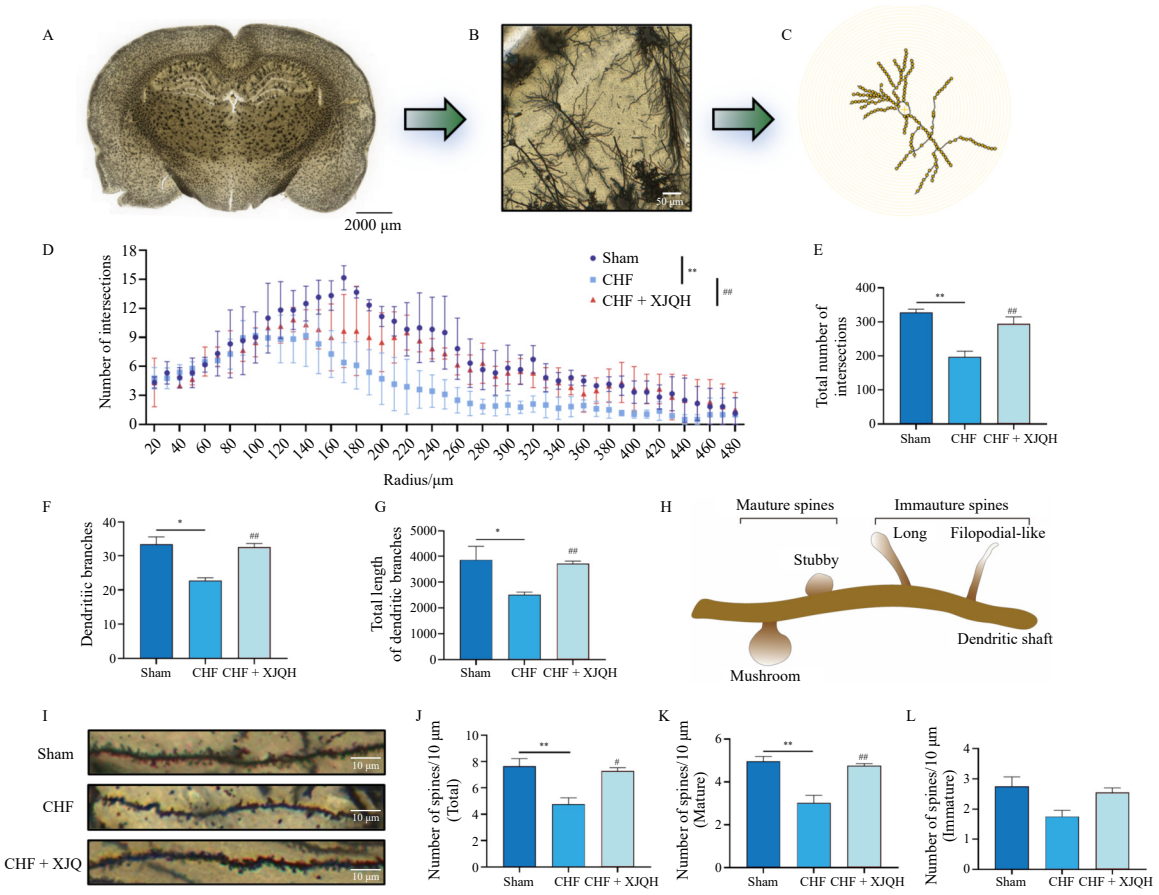

Fig. 7 XJQ promotes the dendritic growth in the hippocampus of CHF rats. (A–C) Examples of reconstructed neurons and dendritic complexity (scale bars: 50 μm). (D) Graphs show the distribution of dendritic intersections at increasing distance from the cell body. (E–G) Quantification data of dendrites, including total number of intersection points (E), the number of dendritic branch (F) and total length of dendritic branches (G). (H) Schematic representation of the classification of dendritic spines. (I) Representative images of dendritic spines in the hippocampus (scale bars: 10 μm). (J–L) Quantification data of total dendritic spines (J), mature dendritic spines (K), immature dendritic spines (L). Data are presented as the mean ± SEM (n = 3); $^{*}P < 0.05$, and $^{**}P < 0.01$ *vs* Sham; $^{\#}P < 0.05$, and $^{\#\#}P < 0.01$ *vs* CHF.

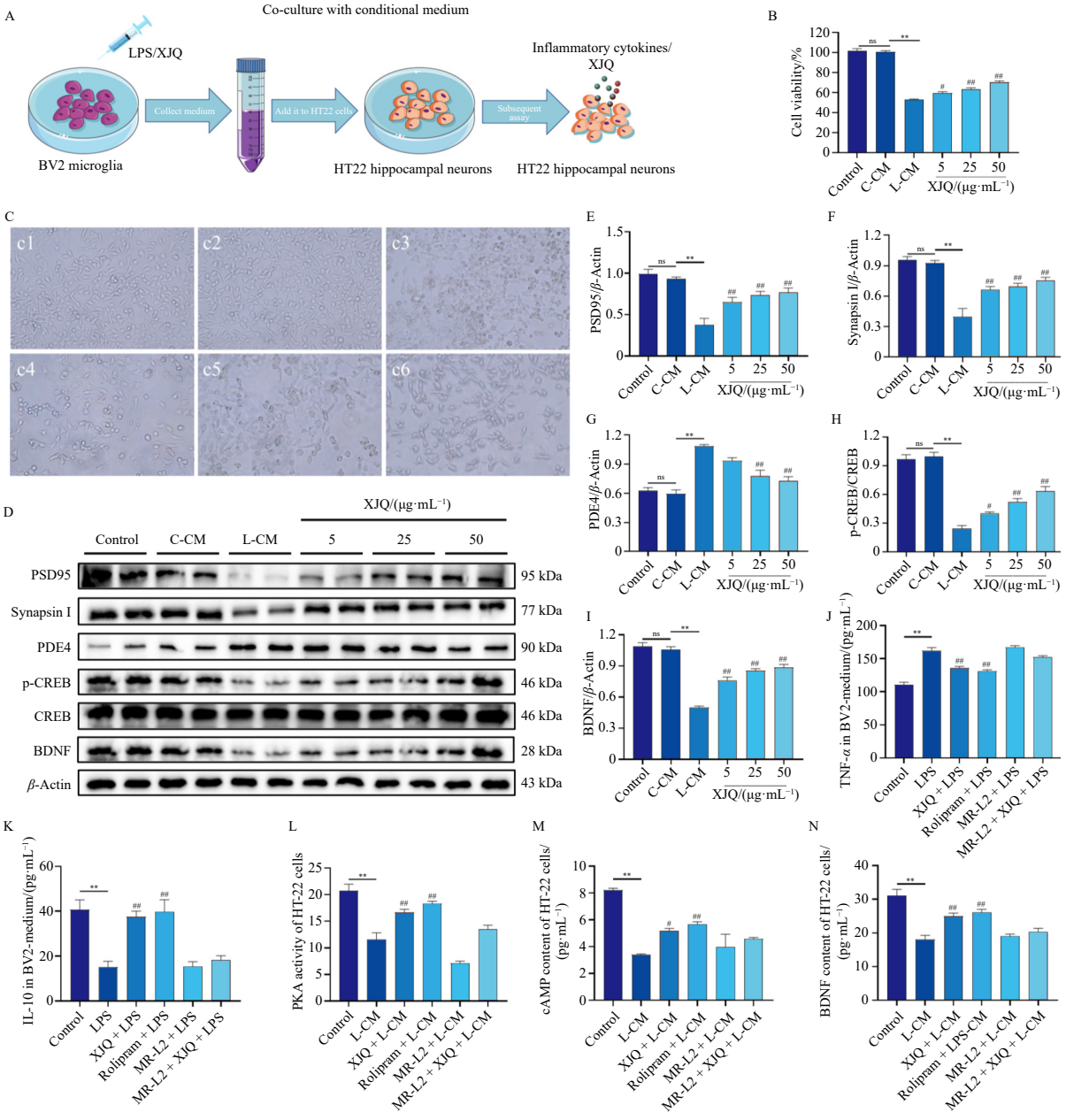

Fig. 8 XJQ mitigates the damage to HT22 hippocampal cells caused by the inflammatory response *via* PDE4-mediated cAMP signaling. BV2 microglial cells were stimulated with LPS and XJQ, followed by the treatment of HT22 cells with BV2 cell-free medium. (A) A simplified overview of a co-culture system featuring BV2 microglia and HT22 hippocampal neurons. (B) The viability of HT22 cells cultured in BV2 cell-free supernatant (n = 6). (C) Representative images of HT22 cells from each group (c1: control, c2: C-CM, c3: L-CM, c4: CM of 5 μg·mL^{-1} XJQ, c5: CM of 25 μg·mL^{-1} XJQ, c6: CM of 50 μg·mL^{-1} XJQ). (D–I) Representative Western blots (D) and quantification data of PSD95 (E), synapsin I (F), PDE4 (G), p-CREB and CREB (H), BDNF (I). β-Actin was used as a loading control (n = 4). (J and K) The levels of TNF-α (J) and IL-10 (K) in BV2 cell-free supernatant. (L–N) The activity of PKA (L), the content of cAMP (M), and the content of BDNF (N) in HT22 homogenate (n = 6). Data are presented as the mean ± SEM; $^{*}P < 0.05$, $^{**}P < 0.01$ *vs* Control; $^{\#}P < 0.05$, and $^{\#\#}P < 0.01$ *vs* LPS. C: control; CM: conditioned medium; L: LPS.

p-CREB levels in HT22 cells (Figs. 8D, and 8G–8H). XJQ treatment successfully reduced PDE4 levels and enhanced p-CREB levels while maintaining stable total CREB protein expression.

To elucidate the critical role of PDE4 in the therapeutic mechanism, rolipram (a PDE4 inhibitor) and MR-L2 (a PDE4 activator) were employed to modulate PDE4 activity. Treatment with XJQ (50 μg·mL^{-1}) decreased TNF-α levels and elevated IL-10 levels, demonstrating effects comparable to rolipram (Figs. 8J and 8K). The combined administration of MR-L2 and XJQ partially diminished the anti-inflammatory effects observed with XJQ alone. These findings suggest that XJQ exerts its anti-inflammatory effects, at least partially, through PDE4 inhibition. Analysis of cAMP signaling-related indicators in HT22 cells treated with different culture media revealed that exposure to L-CM significantly reduced PKA activity, cAMP and BDNF contents (Figs. 8L–8N). XJQ + L-CM enhanced PKA activity, cAMP and BDNF contents in HT-22 cells, demonstrating effects similar to rolipram + L-CM. The combination of MR-L2 with XJQ-treated medium partially reversed the therapeutic effects of XJQ-treated L-CM. These results indicate that XJQ treatment alleviates neuronal and synaptic damage under neuroinflammatory conditions *via* the PDE4-mediated cAMP signaling pathway.

3.9. Key components of XJQ are able to bind to PDE4 protein

PDE4 serves as a critical upstream target for cAMP signaling. Previous studies have demonstrated changes in the PDE4/cAMP/PKA/CREB signaling pathway in the hippocampus following CHF, which XJQ can regulate. To verify the interaction between XJQ's core components and PDE4, molecular docking was performed with all core components against PDE4 (PDB ID: 4MYQ). Intermolecular binding occurs when the binding energy between the

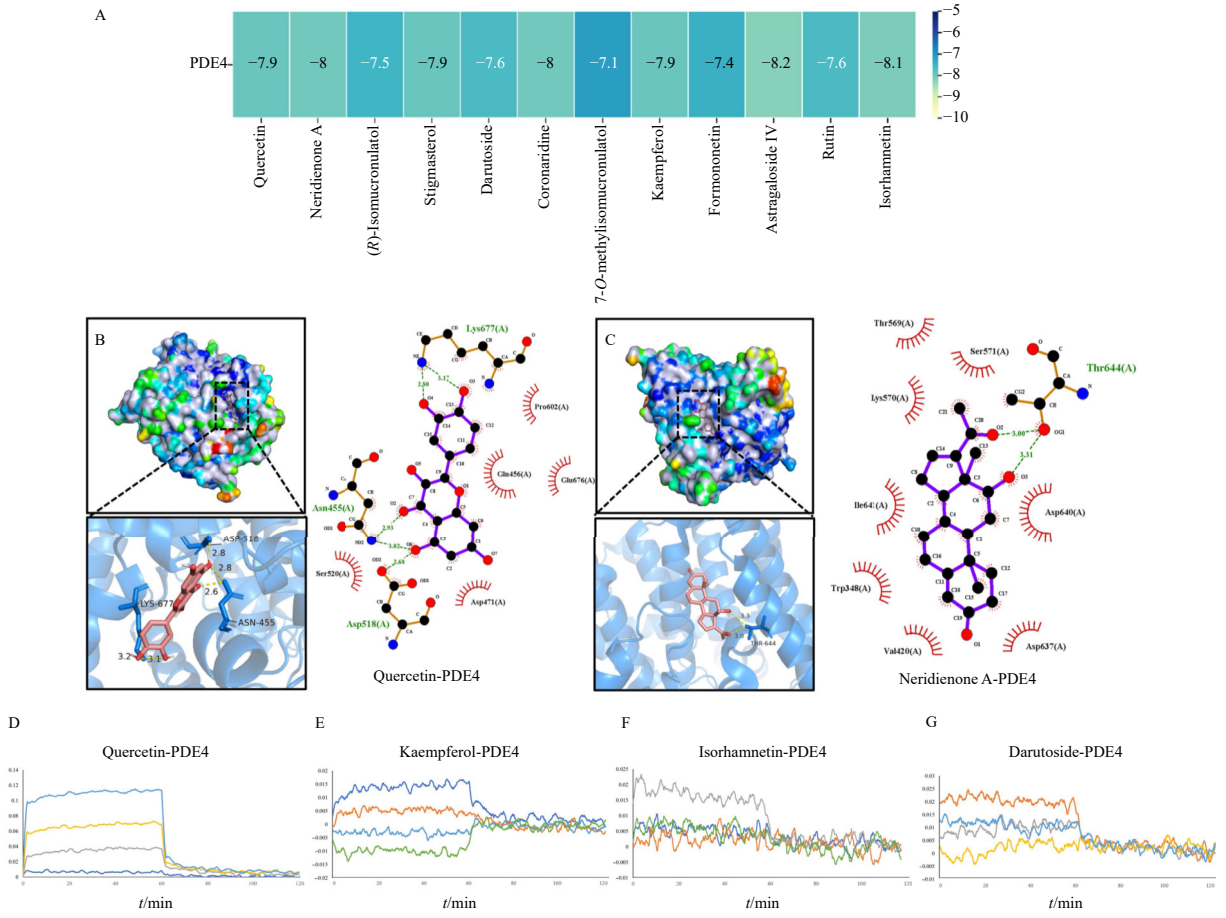

Fig. 9 The key components of XJQ that are able to bind to PDE4 target. (A) A heatmap of binding energies of all core components of XJQ with PDE4, with numbers in the boxes indicating binding energy values for molecular docking. (B and C) Representative molecular docking simulations of two core active components (purple for ligand bonds, green for hydrogen bonds and bond lengths, and brick-red spoke arcs for hydrophobic contacts between ligand and PDE4). (D–G) The binding affinity of the core ingredients of XJQ with PDE4 by BLI assay, including quercetin (D), kaempferol (E), isorhamnetin (F), darutoside (G). BLI: bio-layer interferometry.

ligand and receptor is below 0 kcal·mol^{-1}, with strong intermolecular binding noted below −5 kcal·mol^{-1} [30]. Notably, all core components of XJQ exhibited strong binding affinity to PDE4, with binding energies lower than −5 kcal·mol^{-1} (Fig. 9A). Hydrogen bonding serves a vital role in ligand-receptor interactions by stabilizing the structure, allowing small molecules to bind to receptor proteins, and consequently reducing enzyme activity [31]. All components except stigmasterol, formononetin, and 7-*O*-methylisomucronulatol formed hydrogen bonds with PDE4.

Two representative diagrams of the molecular docking simulation are presented in Figs. 9B and 9C. Each medicinal molecule enters the hydrophobic cavity of PDE4 situated in the predicted protein activity pocket. For example, quercetin forms hydrogen bonds with PDE4 with Asn455, Asp518, and Lys667 residues (Fig. 9B). Neridienone A binds to PDE4 at Thr644, forming two hydrogen bonds of lengths 3.00 and 3.31 Å, respectively (Fig. 9C). BLI assay further validated that quercetin, kaempferol, isorhamnetin, darutoside could directly bind to PDE4 (Figs. 9D–9G). As component concentrations increased, the binding/dissociation curves demonstrated a dose-dependent interaction. The K_d value for quercetin, kaempferol, isorhamnetin, darutoside binding to PDE4 was 2.189 × 10^{-4}, 3.586 × 10^{-5}, 2.872 × 10^{-4}, 9.660 × 10^{-4} mol·L^{-1}, respectively.

4. Discussion

This investigation demonstrates that XJQ treatment effectively alleviates post-CHF cognitive dysfunction *via* suppressing neuroinflammation and promoting dendritic modification and synaptic plasticity in rats. These results highlight the potential therapeutic value of XJQ beyond its traditional clinical application in cardiovascular diseases, specifically addressing post-CHF cognitive impairments.

The research revealed that XJQ substantially improves cardiac function and hemodynamic indices in CHF rats following myocardial infarction. XJQ treatment led to enhanced LVEF, reduced LVEDP, and overall improved hemodynamic stability. Considering the established relationship between CHF and cognitive decline, the observed cardiac improvements likely contribute to cognitive benefits. Current evidence indicates that CHF can negatively affect cognitive function through chronic cerebral hypoperfusion. Reduced cardiac output and elevated LVEDP in CHF patients can result in decreased cerebral blood flow, contributing to cognitive impairments such as memory loss, attention deficits, and executive dysfunction [32, 33]. Consequently, interventions that enhance cardiac function may help ameliorate cognitive decline by restoring adequate cerebral perfusion and reducing ischemic brain injury [34]. XJQ's cardioprotective effects, as demonstrated in this study, may play a significant role in its potential cognitive benefits. By improving cardiac output and reducing LVEDP, XJQ may enhance cerebral blood flow, thereby ensuring sufficient oxygen and nutrient delivery to the brain. This mechanism could mitigate the adverse effects of brain hypoperfusion and support cognitive function.

Furthermore, XJQ's anti-inflammatory properties and ability to promote synaptic plasticity may contribute additional neuroprotective effects. Systemic inflammation represents a common pathobiological characteristic shared between CHF and cognitive

decline [35, 36]. This study identified persistent chronic neuroinflammation in the hippocampus of CHF rats, primarily attributed to activated microglia and astrocytes, aligning with previous research findings [17, 37]. Astrocytes and microglia, which exhibit dynamic morphological and functional properties, continuously monitor neural activity and shape synaptic plasticity, playing essential roles in nervous system development, learning, and memory [38]. Both excessive inhibition and overactivation of microglia reduce spine density, impair excitatory synapse functionality, and alter cortical neuron connectivity, thereby regulating synaptic dynamics [39]. Protoplasmic astrocytes extensively infiltrate neurons and encase synapses [40]. Astrocyte processes engage and disengage from synapses either spontaneously or in response to physiological or pathological stimuli, influencing synaptic morphology [41]. As CHF progresses, glial cells transition to pro-inflammatory microglia and potentially neurotoxic reactive astrocytes, contributing to sympathetic humoral activation and promoting neuronal apoptosis [42]. Microglia-derived IL-1β and TNF-α impair LTP by reducing AMPA receptor phosphorylation [43] and modifying NMDA/AMPA receptor subunit expression [44], thereby enabling microglia to regulate neuroergic synaptic transmission and plasticity.

Moreover, cytokines secreted by microglia and astrocytes directly regulate synapses in the CNS [45]. The findings regarding TNF-α and IL-1β demonstrate significant elevations in the hippocampus post-CHF, consistent with previous studies. IL-10 functions as a crucial anti-inflammatory cytokine. IL-10 levels in the hippocampus remain relatively stable post-CHF. This observation differs from a recent study that reported increased IL-10 levels post-CHF. This discrepancy may arise from temporal differences in IL-10 expression post-CHF, suggesting IL-10 serves a more complex and time-dependent function. XJQ treatment reduces TNF-α and IL-1β levels while increasing IL-10 content in the hippocampus, thereby alleviating neuroinflammation. This study further demonstrated that under inflammatory conditions, CHF induces adverse synaptic alterations, resulting in structural deficiencies in the hippocampus, accompanied by decreased synaptic density and dendritic spine density. XJQ enhances dendrite structure and increases dendritic spine density, particularly mature spines. Co-culture experiments with BV2 microglia and HT22 hippocampal neural cells further validate these findings. These results suggest that impaired synaptic plasticity due to persistent neuroinflammation contributes to post-CHF cognitive dysfunction and offers a therapeutic approach for modulating cerebral immune function to enhance synaptic plasticity.

The therapeutic efficacy of XJQ correlates with its influence on the PDE4-dependent cAMP signaling pathway, as indicated by network pharmacology analysis. This pathway proves essential for cognitive functions, including synaptic plasticity and memory formation. PDE4 belongs to a superfamily of enzymes widely expressed in the brain [46]. PDE4 specifically hydrolyzes cAMP to regulate intracellular cAMP concentration, which significantly influences LTP and synaptic plasticity [47]. cAMP activates PKA, which enhances CREB phosphorylation and promotes BDNF expression to improve cognitive function [48]. Research has shown that PDE4 inhibitors enhance cAMP levels and promote CREB phosphorylation and BDNF expression [48, 49]. This study reveals that CHF triggers increased hippocampal PDE4 expression, resulting in diminished cAMP signaling. The PDE4/cAMP/PKA/CREB pathway may mediate the disruption of neuroplasticity caused by CHF-induced neuroinflammation. XJQ mitigated the increase in PDE4 levels, elevated cAMP content, enhanced PKA activity, and increased BDNF, p-CREB, and synaptic-specific protein expression. Molecular docking and BLI confirm that XJQ's core active components target PDE4 to address cognitive dysfunction. XJQ's effects paralleled those of PDE4 inhibitors, while the PDE4 agonist MR-L2 partially counteracted its therapeutic effects. These findings establish PDE4's crucial role in XJQ-mediated treatment of post-CHF cognitive dysfunction.

The therapeutic efficacy of XJQ in treating CHF and post-CHF cognitive dysfunction stems from its multi-component synergistic mechanism. XXC primarily contains diterpenes and their glycosides, sesquiterpenes, and flavonoids, with diterpenes and their glycosides being considered the most bioactive constituents. Stigmasterol demonstrates cognitive improvement by inhibiting M1 microglia polarization *via* the adenosine 5'-monophosphate-activated protein kinase (AMPK)/NF-κB and AMPK/NLRP3 signaling pathways, thereby reducing microglial inflammatory response to Aβ42 oligomers [50]. The main active components of HQ include saponins, polysaccharides, and flavonoids. Astragaloside IV ameliorates Aβ-induced cognitive impairment, neuroinflammation, and neuronal damage through microglial activation inhibition and NADPH oxidase expression reduction [51]. Astragalus polysaccharide enhances learning and memory in aged rats by increasing phosphorylation levels of *N*-methyl-D-aspartate receptor, calcium/calmodulin-dependent protein kinase II, PKA/CREB, and BDNF [52]. XJP contains C21 steroids, cardiac glycosides, triterpenoids, aldehydes, oligosaccharides, flavonoids, and other compounds, with periosgenin, periplocin, and 4-methoxysalicylaldehyde showing notable activities [53]. Periplocin metabolizes rapidly into periosgenin and periplocymarin *in vivo*, jointly producing inotropic effects [54]. Network pharmacology analysis revealed that 52 XJQ components target 46 cognitive dysfunction-related targets, demonstrating XJQ's multi-component, multi-target, and multi-functional advantages. Notably, certain components, such as quercetin, demonstrate dose-dependent PDE4 inhibition [55], suggesting potential as natural PDE4 selective inhibitors. Astragaloside IV modulates cAMP signaling and improves outcomes in various neurodegenerative and cardiovascular conditions [56, 57]. BLI experiments confirm the significant role of flavonoids including quercetin, kaempferol, isorhamnetin, and glycosides such as darutoside in targeting PDE4, potentially crucial for XJQ's therapeutic effects. This evidence supports XJQ's multi-target and multi-component approach in treating CHF and associated cognitive dysfunctions

In contrast to conventional CHF treatments focusing exclusively on cardiac symptoms, XJQ addresses both cardiac dysfunction and cognitive impairments, offering a more comprehensive therapeutic approach. This integrated strategy presents significant clinical advantages by incorporating neuropsychiatric aspects typically overlooked in conventional treatments. Moreover, the integration of XJQ with standard therapies could advance CHF management strategies, enabling a more holistic approach to patient care. XJQ's dual action on cardiac and cognitive symptoms facilitates more comprehensive treatment strategies, potentially reducing CHF burden and enhancing treatment adherence.

However, several aspects require further investigation. Additional research is needed to fully elucidate the specific XJQ components responsible for treating CHF and post-CHF cognitive dysfunction. While this study emphasized structural synaptic plasticity, understanding XJQ's effects on functional synaptic plasticity, including LTP and long-term depression, remains crucial for future research. Furthermore, investigation of XJQ's long-term efficacy is necessary to evaluate its clinical relevance and safety profile. Future research should prioritize clinical trials to validate XJQ's efficacy and safety in human CHF populations. Additionally, examining dose-response relationships and long-term effects of XJQ on cognitive function in CHF patients remains essential.

In conclusion, this study demonstrates that XJQ improves cardiac function, subsequently enhancing cognitive performance in CHF rats. Additionally, XJQ directly alleviates learning and

memory impairment *via* suppressing hippocampal neuroinflammation and promoting synaptic plasticity through the PDE4/cAMP/PKA/CREB pathway (Fig. 10). XJQ thus delivers synergistic benefits for both cardiac and cognitive function.

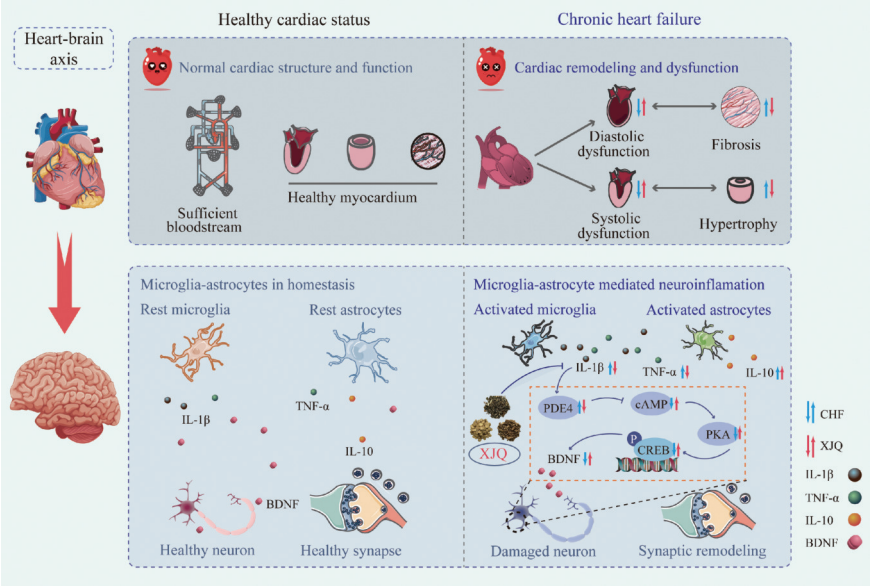

Fig. 10 Mechanism of XJQ in enhancing post-CHF cognitive function by inhibiting neuroinflammation and promoting synaptic plasticity *via* regulating the PDE4/cAMP/PKA/CREB pathway.

Funding

This work was supported by the National Natural Science Foundation of China (Nos. 82430116 and 82574622), the Special Fund of Central Committee High Level Chinese Medicine Hospital (Nos. DZMG-LJRC-0014, DZMG-ZJXY-23013), Chinese Medicine Inheritance and Innovation "Thousand Million" Talents Project (Qihuang Project 2021) Qihuang Scholars; the Medical and Health Industry Development Project of Tongzhou District (2023).

Availability of data and materials

The datasets analyzed during the current study are available from the corresponding author on reasonable request.

Acknowledgments

We used some free design elements in Fig. 10 from www.vecteezy.com. Thanks to the website for the high-quality figure elements.

Declaration of competing interest

These authors have no conflict of interest to declare.

References

1 Maroofi A, Moro T, Agrimi J, et al. Cognitive decline in heart failure: biomolecular mechanisms and benefits of exercise. *Biochim Biophys Acta Mol Basis Dis*. 2022;1868(11):166511. https://doi.org/10.1016/j.bbadis.2022.166511.

2 Doehner W, Čelutkienė J, Yilmaz MB, et al. Heart failure and the heart-brain axis. *QJM*. 2023;116(11):897-902. https://doi.org/10.1093/qjmed/hcad179.

3 McDonagh TA, Metra M, Adamo M, et al. 2021 ESC guidelines for the diagnosis and treatment of acute and chronic heart failure: developed by the task force for the diagnosis and treatment of acute and chronic heart failure of the European Society of Cardiology (ESC). With the special contribution of the Heart Failure Association (HFA) of the ESC. *Eur J Heart Fail*. 2022;24(1):4-131. https://doi.org/10.1002/ejhf.2333.

4 Rigueira J, Agostinho JR, Aguiar-Ricardo I, et al. Heart and brain interactions in heart failure: cognition, depression, anxiety, and related outcomes. *Rev Port Cardiol (Engl Ed)*. 2021;40(8):547-555. https://doi.org/10.1016/j.repc.2020.09.009.

5 Ye S, Huynh Q, Potter EL. Cognitive dysfunction in heart failure: pathophysiology and implications for patient management. *Curr Heart Fail Rep*. 2022;19(5):303-315. https://doi.org/10.1007/s11897-022-00564-z.

6 Liu J, Xiao G, Liang Y, et al. Heart-brain interaction in cardiogenic dementia: pathophysiology and therapeutic potential. *Front Cardiovasc Med*. 2024;11:1304864. https://doi.org/10.3389/fcvm.2024.1304864.

7 Soleimani H, Nasrollahizadeh A, Hajiqasemi M, et al. Comparative analysis of treatment options for chronic heart failure and depression: a systematic review and Bayesian network meta-analysis. *Heart Fail Rev*. 2024;29(4):841-852. https://doi.org/10.1007/s10741-024-10403-z.

8 Gilstrap L, Cohen A, Ouellet GM, et al. The association between beta-blockers and outcomes in patients with heart failure and concurrent Alzheimer's disease and related dementias. *J Am Geriatr Soc*. 2023;71(2):404-413. https://doi.org/10.1111/jgs.18086.

9 Luo Z, Yin F, Wang X, et al. Progress in approved drugs from natural product resources. *Chin J Nat Med*. 2024;22(3):195-211. https://doi.org/10.1016/S1875-5364(24)60582-0.

10 Zhao D, Guo K, Zhang Q, et al. Mechanism of XiJiaQi in the treatment of chronic heart failure: integrated analysis by pharmacoinformatics, molecular dynamics simulation, and SPR validation. *Comput Biol Med*. 2023;166:107479. https://doi.org/10.1016/j.compbiomed.2023.107479.

11 Wei XH, Liu WJ, Jiang W, et al. XinLi Formula, a traditional Chinese decoction, alleviates chronic heart failure *via* regulating the interaction of AGTR1 and AQP1. *Phytomedicine*. 2023;113:154722. https://doi.org/10.1016/j.phymed.2023.154722.

12 Yang T, Lu Z, Wang L, et al. Dynamic changes in brain glucose metabolism and neuronal structure in rats with heart failure. *Neuroscience*. 2020;424:34-44. https://doi.org/10.1016/j.neuroscience.2019.10.008.

13 Reagan-Shaw S, Nihal M, Ahmad N. Dose translation from animal to human studies revisited. *FASEB J*. 2008;22(3):659-661. https://doi.org/10.1096/fj.07-9574LSF.

14 Feng J, Guo J, Yan J, et al. Luhong Formula and hydroxysafflor yellow A protect cardiomyocytes by inhibiting autophagy. *Phytomedicine*. 2023;110:154636. https://doi.org/10.1016/j.phymed.2022.154636.

15 Fei Q, Ma H, Zou J, et al. Metformin protects against ischaemic myocardial injury by alleviating autophagy-ROS-NLRP3-mediated inflammatory response in macrophages. *J Mol Cell Cardiol*. 2020;145:1-13. https://doi.org/10.1016/j.yjmcc.2020.05.016.

16 Lu Z, Yang T, Wang L, et al. Comparison of different protocols of Morris water maze in cognitive impairment with heart failure. *Brain Behav*. 2020;10(2):e01519. https://doi.org/10.1002/brb3.1519.

17 Sun N, Mei Y, Hu Z, et al. Ghrelin attenuates depressive-like behavior, heart failure, and neuroinflammation in postmyocardial infarction rat model. *Eur J Pharmacol*. 2021;901:174096. https://doi.org/10.1016/j.ejphar.2021.174096.

18 Ru J, Li P, Wang J, et al. TCMSP: a database of systems pharmacology for drug discovery from herbal medicines. *J Cheminform*. 2014;6:13. https://doi.org/10.1186/1758-2946-6-13.

19 Zhu X, Liu J, Huang S, et al. Neuroprotective effects of isoliquiritigenin against cognitive impairment *via* suppression of synaptic dysfunction, neuronal injury, and neuroinflammation in rats with kainic acid-induced seizures. *Int Immunopharmacol*. 2019;72:358-366. https://doi.org/10.1016/j.intimp.2019.04.028.

20 Li YS, Zhang J, Tian GH, et al. Kirenol, darutoside and hesperidin contribute to the anti-inflammatory and analgesic activities of *Siegesbeckia pubescens* Makino by inhibiting COX-2 expression and inflammatory cell infiltration. *J Ethnopharmacol*. 2021;268:113547. https://doi.org/10.1016/j.jep.2020.

113547.
21 Sun XY, Li LJ, Dong QX, et al. Rutin prevents Tau pathology and neuroinflammation in a mouse model of Alzheimer's disease. *J Neuroinflammation*. 2021;18(1):131. https://doi.org/10.1186/s12974-021-02182-3.
22 Chu JMT, Abulimiti A, Wong BSH, et al. *Sigesbeckia orientalis* L. derived active fraction ameliorates perioperative neurocognitive disorders through alleviating hippocampal neuroinflammation. *Front Pharmacol*. 2022;13:846631. https://doi.org/10.3389/fphar.2022.846631.
23 Sakuma S, Kawanishi S, Shoji J. Constituents of the Chinese crude drug "Wujiapi". IX. Structure of glycoside H2 a potentiator of NGF-mediated nerve fiber outgrowth. *Chem Pharm Bull (Tokyo)*. 1980;28(1):163-168. https://doi.org/10.1248/cpb.28.163.
24 Santos RAS, Sampaio WO, Alzamora AC, et al. The ACE2/angiotensin-(1-7)/MAS axis of the renin-angiotensin system: focus on angiotensin-(1-7). *Physiol Rev*. 2018;98(1):505-553. https://doi.org/10.1152/physrev.00023.2016.
25 Obradovic DM, Büttner P, Rommel KP, et al. Soluble ST2 receptor: biomarker of left ventricular impairment and functional status in patients with inflammatory cardiomyopathy. *Cells*. 2022;11(3):414. https://doi.org/10.3390/cells11030414.
26 Smith SW. Reticular and areticular Nissl bodies in sympathetic neurons of a lizard. *J Biophys Biochem Cytol*. 1959;6(1):77-84. https://doi.org/10.1083/jcb.6.1.77.
27 Lei T, Li Y, Song Y, et al. ADMET evaluation in drug discovery: 15. Accurate prediction of rat oral acute toxicity using relevance vector machine and consensus modeling. *J Cheminform*. 2016;8:6. https://doi.org/10.1186/s13321-016-0117-7.
28 Costello A, Linning-Duffy K, Vandenbrook C, et al. Effects of bright light therapy on neuroinflammatory and neuroplasticity markers in a diurnal rodent model of seasonal affective disorder. *Ann Med*. 2023;55(2):2249015. https://doi.org/10.1080/07853890.2023.2249015.
29 Zaccard CR, Gippo I, Song A, et al. Dendritic spinule-mediated structural synaptic plasticity: implications for development, aging, and psychiatric disease. *Front Mol Neurosci*. 2023;16:1059730. https://doi.org/10.3389/fnmol.2023.1059730.
30 Hsin KY, Ghosh S, Kitano H. Combining machine learning systems and multiple docking simulation packages to improve docking prediction reliability for network pharmacology. *PLoS One*. 2013;8(12):e83922. https://doi.org/10.1371/journal.pone.0083922.
31 Trasatti JP, Woo J, Ladiwala A, et al. Rational design of peptide affinity ligands for the purification of therapeutic enzymes. *Biotechnol Prog*. 2018;34(4):987-998. https://doi.org/10.1002/btpr.2637.
32 Shin MS, An M, Kim S, et al. Concomitant diastolic dysfunction further interferes with cognitive performance in moderate to severe systolic heart failure. *PLoS One*. 2017;12(10):e0184981. https://doi.org/10.1371/journal.pone.0184981.
33 Ovsenik A, Podbregar M, Fabjan A. Cerebral blood flow impairment and cognitive decline in heart failure. *Brain Behav*. 2021;11(6):e02176. https://doi.org/10.1002/brb3.2176.
34 van Nieuwkerk AC, Delewi R, Wolters FJ, et al. Cognitive impairment in patients with cardiac disease: implications for clinical practice. *Stroke*. 2023;54(8):2181-2191. https://doi.org/10.1161/STROKEAHA.123.040499.
35 Murphy SP, Kakkar R, McCarthy CP, et al. Inflammation in heart failure: JACC state-of-the-art review. *J Am Coll Cardiol*. 2020;75(11):1324-1340. https://doi.org/10.1016/j.jacc.2020.01.014.
36 Md Pisar M, Chee BJ, Long I, et al. Protective effects of *Centella asiatica* extract on spatial memory and learning deficits in animal model of systemic inflammation induced by lipopolysaccharide. *Ann Med*. 2023;55(1):2224970. https://doi.org/10.1080/07853890.2023.2224970.
37 Ge Y, Xu W, Zhang L, et al. Ginkgolide B attenuates myocardial infarction-induced depression-like behaviors *via* repressing IL-1β in central nervous system. *Int Immunopharmacol*. 2020;85:106652. https://doi.org/10.1016/j.intimp.2020.106652.
38 Allen NJ, Lyons DA. Glia as architects of central nervous system formation and function. *Science*. 2018;362(6411):181-185. https://doi.org/10.1126/science.aat0473.
39 Miyamoto A, Wake H, Ishikawa AW, et al. Microglia contact induces synapse formation in developing somatosensory cortex. *Nat Commun*. 2016;7:12540. https://doi.org/10.1038/ncomms12540.
40 Bernardinelli Y, Randall J, Janett E, et al. Activity-dependent structural plasticity of perisynaptic astrocytic domains promotes excitatory synapse stability. *Curr Biol*. 2014;24(15):1679-1688. https://doi.org/10.1016/j.cub.2014.06.025.
41 Panatier A, Theodosis DT, Mothet JP, et al. Glia-derived D-serine controls NMDA receptor activity and synaptic memory. *Cell*. 2006;125(4):775-784. https://doi.org/10.1016/j.cell.2006.02.051.
42 Althammer F, Ferreira-Neto HC, Rubaharan M, et al. Three-dimensional morphometric analysis reveals time-dependent structural changes in microglia and astrocytes in the central amygdala and hypothalamic paraventricular nucleus of heart failure rats. *J Neuroinflammation*. 2020;17(1):221. https://doi.org/10.1186/s12974-020-01892-4.
43 Liu M, Li J, Dai P, et al. Microglia activation regulates GluR1 phosphorylation in chronic unpredictable stress-induced cognitive dysfunction. *Stress*. 2015;18(1):96-106. https://doi.org/10.3109/10253890.2014.995085.
44 Riazi K, Galic MA, Kentner AC, et al. Microglia-dependent alteration of glutamatergic synaptic transmission and plasticity in the hippocampus during peripheral inflammation. *J Neurosci*. 2015;35(12):4942-4952. https://doi.org/10.1523/JNEUROSCI.4485-14.2015.
45 Zipp F, Bittner S, Schafer DP. Cytokines as emerging regulators of central nervous system synapses. *Immunity*. 2023;56(5):914-925. https://doi.org/10.1016/j.immuni.2023.04.011.
46 Richter W, Menniti FS, Zhang HT, et al. PDE4 as a target for cognition enhancement. *Expert Opin Ther Targets*. 2013;17(9):1011-1027. https://doi.org/10.1517/14728222.2013.818656.
47 Burgin AB, Magnusson OT, Singh J, et al. Design of phosphodiesterase 4D (PDE4D) allosteric modulators for enhancing cognition with improved safety. *Nat Biotechnol*. 2010;28(1):63-70. https://doi.org/10.1038/nbt.1598.
48 Bruno O, Fedele E, Prickaerts J, et al. GEBR-7b, a novel PDE4D selective inhibitor that improves memory in rodents at non-emetic doses. *Br J Pharmacol*. 2011;164(8):2054-2063. https://doi.org/10.1111/j.1476-5381.2011.01524.x.
49 Titus DJ, Sakurai A, Kang Y, et al. Phosphodiesterase inhibition rescues chronic cognitive deficits induced by traumatic brain injury. *J Neurosci*. 2013;33(12):5216-5226. https://doi.org/10.1523/JNEUROSCI.5133-12.2013.
50 Jie F, Yang X, Yang B, et al. Stigmasterol attenuates inflammatory response of microglia *via* NF-κB and NLRP3 signaling by AMPK activation. *Biomed Pharmacother*. 2022;153:113317. https://doi.org/10.1016/j.biopha.2022.113317.
51 Chen F, Yang D, Cheng XY, et al. Astragaloside IV ameliorates cognitive impairment and neuroinflammation in an oligomeric Aβ induced alzheimer's disease mouse model *via* inhibition of microglial activation and NADPH oxidase expression. *Biol Pharm Bull*. 2021;44(11):1688-1696. https://doi.org/10.1248/bpb.b21-00381.
52 Yao H, Gu LJ, Guo JY. Study on effect of Astragali Radix polysaccharides in improving learning and memory functions in aged rats and its mechanism. *Chin J Chin Mater Med*. 2014;39(11):2071-2075. https://doi.org/10.4268/cjcmm20141125.
53 Yang X, Li MY, Yan CY, et al. Research progress on chemical composition and pharmacological effects of Periplocae Cortex and predictive analysis on Q-marker. *Chin J Chin Mater Med*. 2020;45(12):2772-2783. https://doi.org/10.19540/j.cnki.cjcmm.20200327.202.
54 Liang S, Deng F, Xing H, et al. P-glycoprotein- and organic anion-transporting polypeptide-mediated transport of periplocin may lead to drug-herb/drug-drug interactions. *Drug Des Devel Ther*. 2014;8:475-483. https://doi.org/10.2147/DDDT.S61024.
55 Townsend EA, Emala CW. Quercetin acutely relaxes airway smooth muscle and potentiates *β*-agonist-induced relaxation *via* dual phosphodiesterase inhibition of PLCβ and PDE4. *Am J Physiol Lung Cell Mol Physiol*. 2013;305(5):L396-403. https://doi.org/10.1152/ajplung.00125.2013.
56 Du Q, Zhang S, Li A, et al. Astragaloside IV inhibits adipose lipolysis and reduces hepatic glucose production *via* Akt dependent PDE3B expression in HFD-Fed mice. *Front Physiol*. 2018;9:15. https://doi.org/10.3389/fphys.2018.00015.
57 Ye Q, Su L, Chen D, et al. Astragaloside IV induced miR-134 expression reduces EMT and increases chemotherapeutic sensitivity by suppressing CREB1 signaling in colorectal cancer cell line SW-480. *Cell Physiol Biochem*. 2017;43(4):1617-1626. https://doi.org/10.1159/000482025.